Ctf4 organizes sister replisomes and Pol α into a replication factory

Zuanning Yuan[1], Roxana Georgescu[2,3], Ruda de Luna Almeida Santos[1], Daniel Zhang[3], Lin Bai[1], Nina Y. Yao[3], Gongpu Zhao[4], Michael E. O'Donnell[2,3*], Huilin Li[1*]

[1] Structural Biology Program, Van Andel Research Institute, Grand Rapids, Michigan, USA

[2] Howard Hughes Medical Institute

[3] DNA Replication Laboratory, The Rockefeller University, New York, New York, USA 10065

[4] David Van Andel Advanced Cryo-EM Suite, Van Andel Research Institute, Grand Rapids, Michigan, USA 49503

[*]Equal corresponding authors. Correspondence should be addressed to M.O.D. (odonnel@rockefeller.edu) or H.L. (Huilin.Li@vai.org)

Key words: replication factory, sister replication forks, Ctf4/AND1, DNA replication, CMG helicase.

ABSTRACT

The current view is that eukaryotic replisomes are independent. Here we show that Ctf4 tightly dimerizes CMG helicase, with an extensive interface involving Psf2, Cdc45, and Sld5. Interestingly, Ctf4 binds only one Pol α-primase. Thus, Ctf4 may have evolved as a trimer to organize two helicases and one Pol α-primase into a replication factory. In the 2CMG-Ctf4$_3$-1Pol α-primase factory model, the two CMGs nearly face each other, placing the two lagging strands toward the center and two leading strands out the sides. The single Pol α-primase is centrally located and may prime both sister replisomes. The Ctf4-coupled-sister replisome model is consistent with cellular microscopy studies revealing two sister forks of an origin remain attached and are pushed forward from a protein platform. The replication factory model may facilitate parental nucleosome transfer during replication.

INTRODUCTION

Replication of cellular genomes requires numerous proteins that work together in a replisome. Replication in eukaryotes utilize CMG helicase (Cdc45–Mcm2-7–GINS) (Ilves et al., 2010; Moyer et al., 2006; Costa et al, 2011), leading and lagging strand DNA polymerases (Pol) ε and δ, Pol α-primase, PCNA clamps, the RFC clamp loader, and numerous accessory factors of less defined function (Bell and Labib, 2016; Burgers and Kunkel, 2017). Replication in eukaryotes is performed in localized foci in nuclei that contain 10-100 replication forks (Falaschi, 2000; Kitamura et al., 2006). Recent super resolution microscopy has resolved these foci into single replicon factories from bidirectional origins (Chagin et al., 2016; Saner et al., 2013). Nuclear foci in the budding yeast, *Saccharomyces cerevisae*, most often contain only single replicon factories having two replication forks, although some foci consist of more than two replication forks (Saner et al., 2013). The molecular structure of a single core replicon factory unit, consisting of two replication forks is unknown, but several studies demonstrate that sister replication forks remain together during S phase (Conti et al., 2007; Falaschi, 2000; Ligasova et al., 2009; Natsume and Tanaka, 2010), and that sister double-strand (ds) DNA products are extruded in loops directed away from a replication protein scaffold (Gillespie and Blow, 2010; Saner et al., 2013).

Ctf4 (Chromosome Transmission Fidelity 4) is a homo-trimer (Ctf4$_3$) that connects Pol α-primase and CMG helicase (Gambus et al., 2009; Miles and Formosa, 1992; Simon et al., 2014; Tanaka et al., 2009a). Previous EM studies reveal that Ctf4$_3$–Pol α-primase resides on the opposite side of CMG from the leading strand DNA polymerase (Pol) ε in an individual replisome (Sun et al., 2015) (**Figure 1a**). Ctf4 also transiently binds Dna2, Dpb2, Tof2 and Chl1, and thus Ctf4 is proposed to be a dynamic hub (Villa et al., 2016; Samora et al., 2016). Dynamic interaction enables multiple factors binding through time-sharing on Ctf4 and occurs through a conserved Ctf4-Interaction Peptide (CIP) motif (Kilkenny et al., 2017; Samora et al., 2016; Simon et al., 2014; Villa et al., 2016). The structures of the C-half of Ctf4 and its human orthologue AND1 reveal a disc-shaped constitutive trimer via the β-propeller domains on the N-terminal face (N-face) with the three C-terminal helical domains interacting with up to three CIP peptides on the C-face (Kilkenny et al., 2017; Simon et al., 2014). Ctf4 mutants that disrupt connection to CMG are deficient in transfer of parental nucleosomes to the lagging strand daughter duplex, with implications for a role in epigenetic inheritance during development (Gan et al., 2018). In human, AND1 (hCMG) also binds CMG and is important for replication progression and DNA repair (Kang et al., 2013; Abe et al., 2018; Williams and McIntosh, 2002; Yoshizawa-Sugata and Masai, 2009).

Earlier structure studies of Ctf4 used subassemblies of CMG and Pol α-primase (Simon et al., 2014), and thus it has not been fully understood how Ctf4 interacts with the holoenzyme forms of CMG and Pol α-primase, and whether Ctf4 might bind two Pol α-primase as proposed (**Figure 1a**). We sought to address these questions by a combination of biochemistry and cryo-EM and found that one Ctf4$_3$ binds CMG very tight, not dynamic, and can bind 1, 2, or 3 CMG holoenzymes without steric hinderance at a

120° angle to one another. We also determine a structure of $Ctf4_3$ bound to Pol α-primase and observe $Ctf4_3$ binds only one copy of Pol α-primase. We have reconstituted a 2CMG-2Pol ε–1$Ctf4_3$–1Pol α-primase complex biochemically and can visualize a 2CMG–1$Ctf4_3$–1Pol α-primase complex by EM. Moreover, the CMGs retain helicase activity while multimerized by $Ctf4_3$. These findings led us to propose that sister-replisomes are coupled by $Ctf4_3$ in a "replication factory" of 2CMG-Pol ε–1$Ctf4_3$–1Pol α-primase (**Figure 1b**). We further address in the Discussion how various CIP factors may bind the replication factory, how Pol α-primase may be utilized for lagging strand priming of sister replication forks, and implications of a factory for parental nucleosome transfer to daughter duplexes. We note that these *in vitro* findings require cellular validation, which will be pursued in a separate study.

RESULTS

CMG-Ctf4 form a stable complex. To explore how $Ctf4_3$ interacts with replisome factors we performed glycerol gradient sedimentation of protein mixtures (**Figure 2 – figure supplement 1**). This method originally revealed that Pol ε binds CMG, forming a CMG-Pol ε complex that sediments faster than either component alone (compare panels c and h with panel d) (Langston et. al., 2014). CMG binding to $Ctf4_3$ was also readily apparent (compare panels c and g with panel e). It was initially surprising that the CMG-$Ctf4_3$ complex migrated heavier than CMG-Pol ε, even though $Ctf4_3$ is not quite as large as Pol ε, because studies in the human system indicated there was only room for one CMG on Ctf4 (Kang et al., 2013), consistent with an earlier proposal (Simon et al., 2014) (**Figure 2 - figure supplement 1**, compare panels d and e).

To study the CMG-$Ctf4_3$ complex further we mixed $Ctf4_3$ and CMG and applied it to a MonoQ ion exchange column; a complex of CMG-$Ctf4_3$ eluted at >400 mM NaCl (**Figure 2a**). This result indicated CMG-$Ctf4_3$ is a stable complex, and is not loose, consistent with an apparent tighter interaction of GINS complex to $Ctf4_3$ compared to the CIP peptide of Sld5 (Simon et al., 2014). The MonoQ isolated CMG-$Ctf4_3$ complex was also stable to size-exclusion chromatography (SEC) (**Figure 2b**). We conclude that CMG is tightly bound and highly stable on the $Ctf4_3$ hub. Density scans of fractions within the SEC elution profile indicated a heterogeneous mixture of CMG-$Ctf4_3$ complexes, with CMG:$Ctf4_3$ ratios ranging from 3:1 to 1:1. We therefore examined different fractions by cryoEM and found that indeed, more than one CMG can bind $Ctf4_3$, as described below.

Structure of the 1CMG-$Ctf4_3$ complex. To investigate the structural basis underlying the strength of the CMG-$Ctf4_3$ complexes, we determined the structure of the 1CMG-$Ctf4_3$ complex by cryo-EM to 3.9-Å resolution**.** In agreement with previous structural studies of CMG (Abid Ali et al., 2016; Yuan et al., 2016), the C-tier AAA+ ring of Mcm2-7 is highly dynamic. By excluding this region in 3D refinement, we improved the 3D map of 1CMG-$Ctf4_3$ to 3.8-Å resolution (**Figure 3a-c, Table 1, Figure 3 - figure supplements 1 and 2**).

Based on the density features, as well as previously reported separate structures of $Ctf4_3$ and CMG (Simon et al., 2014; Yuan et al., 2016), we built an atomic model (**Figures 3, 4, and Figure 4 - figure supplement 1, Video 1**). The overall architecture reveals an extensive interface between the helicase and $Ctf4_3$, amounting to 1706 $Å^2$ of buried area, larger than the stable contact between Cdc45 and Mcm2-7 (1182 $Å^2$) and between GINS and Mcm2-7 (1583 $Å^2$), explaining the stability of the CMG-$Ctf4_3$ complex. Interestingly, there is a wide gap between Ctf4 and the Sld5 subunit of CMG that contains the CIP peptide (**Figure 4a**).

There are three interfaces between CMG and $Ctf4_3$, involving 3 different subunits of CMG with one protomer of $Ctf4_3$ (**Figure 4c,d,e; Figure 4 - figure supplement 2**). The two major interfaces are

between the β-propeller region of Ctf4 and both the Cdc45 subunit of CMG (**Figure 4c**) and the Psf2 subunit in the GINS complex of CMG (**Figure 4d**); these interfaces were previously uncharacterized. The interactions between Cdc45 and the Ctf4 propeller are largely electrostatic, involving several salt bridges and hydrogen bonds. Furthermore, a loop connecting strands β1 and β2 of Psf2, disordered in the CMG structure in the absence of $Ctf4_3$ (Yuan et al., 2016), inserts into two blades of the β-propeller and becomes ordered by forming multiple interactions (**Figure 4d**). The interface between Psf2 and Ctf4 involves H-bonds between Psf2 residues Arg34 and Lys36 with Ctf4 residues Asn850 and Tyr848, respectively, as well as hydrophobic interaction among Ctf4 residues Phe518, Leu770, and Pro771 and Psf2 residues Ile27, Phe28, and Pro29. As expected, the main Ctf4-contacting regions of Cdc45, Psf2 are well conserved across evolution (**Figure 4 – figure supplement 3**). The previously-identified interaction between Ctf4 and the CIP peptide in the Sld5 subunit (Simon et al., 2014) of the GINS complex is actually a minor interaction site in which the N-terminal residues 3–15 of Sld5 form a short helix that bundles with the helical domain of Ctf4, primarily via a hydrophobic interface (**Figure 4e**). An intervening long peptide (aa 16 -53) of Sld5 is disordered. This long flexible linker to the CIP peptide of Sld5 may explain why the CIP peptide of Sld5 is not required to observe CMG binding to Ctf4 in cells, predicting a second tethering point between CMG and Ctf4 (Simon et al., 2014). Therefore the Psf2 and Cdc45 extensive interfaces explain the stable association between Ctf4 and CMG.

The 2CMG-$Ctf4_3$ and 3CMG-$Ctf4_3$ complexes. CryoEM 2D averages of two CMGs bound to $Ctf4_3$ show the CMGs are held rigidly, consistent with their stable binding to $Ctf4_3$ (**Figure 5a**). The 3D reconstruction shows each CMG interacts with only one protomer of $Ctf4_3$, and the CMG contact is limited to one side of the $Ctf4_3$ triangle related by 120° (**Figure 5b**). While earlier 2D studies of Ctf4 binding the GINS subassembly also observed a similar geometry, it has been thought that only one large CMG holoenzyme could bind Ctf4 (Kang et al., 2013; Simon et. al, 2014). However the structure of 2CMG-$Ctf4_3$ shows that the large CMGs do not sterically obstruct one another. Therefore, one $Ctf4_3$ may organize up to three CMGs. Indeed, we observed 2D class averages that show two or three CMGs per $Ctf4_3$, related by the three-fold axis of $Ctf4_3$ **(Figure 5a, Figure 5 - figure supplements 1 and 2**). We determined the cryo-EM 3D maps of the 2CMG-$Ctf4_3$ complex at 5.8 Å resolution (**Figure 5b, Figure 5 – figure supplement 1, Video 2**) and the 3CMG-$Ctf4_3$ complex at 7.0 Å (**Figure 5 – figure supplement 2**), respectively. The interactions between individual CMG helicases and their respective partner Ctf4 protomers in both 2CMG-$Ctf4_3$ and 3CMG-$Ctf4_3$ complexes are virtually identical, the same as in the 1CMG-$Ctf4_3$ complex described above, consistent with no steric clash between the CMGs.

Considering that the 2CMG-$Ctf4_3$ complex may be more physiologicaly relevant, as factories consisting of two forks straddling one origin are observed in vivo (Saner et al., 2013), and a 2CMG occupancy of $Ctf4_3$ leaves one protomer of $Ctf4_3$ for other CIP factors such as Pol α-primase, we continue this report in the context of the 2CMG-$Ctf4_3$ complex.

The key insight from the 2CMG-$Ctf4_3$ structure is that the two CMGs are held on the same side – the top side, or the N-face of the disc-shaped $Ctf4_3$ when the structure is viewed from the side of the $Ctf4_3$ disk (**Figure 5b**). Hence, the two N-tier rings of the Mcm2-7 hexamers – where the dsDNAs approach for dsDNA unwinding (Georgescu et al., 2017; Douglas et al., 2018) – approximately face one another at an angle of 120° and the C-tier motor rings of the two CMGs, where the leading strand Pol ε's bind (Sun et al., 2015), face outwards and away from each other.

A 1:1 complex of $Ctf4_3$ and Pol α-primase. Earlier studies observed only one Pol α-primase bound to $Ctf4_3$ (Simon et al., 2014) (see their Fig. 4e and Extended data Figs. 8 and 9). We wished to understand

the basis of this stoichiometry but the interaction of $Ctf4_3$ to Pol α-primase was too loose to isolate a complex for cryoEM analysis, consistent with the dynamic hub model of $Ctf4_3$ (Simon et al., 2014; Villa et al., 2016). Thus we directly mixed Pol α-primase and $Ctf4_3$ at 1:1 and 3:1 molar ratios followed by cryoEM analysis to study how Pol α-primase binds $Ctf4_3$ in the absence of CMG.

We first examined Pol α-primase alone and found Pol α-primase was flexible when frozen in vitreous ice, and did not generate well-defined 2D class averages. But under negative-stain EM conditions, Pol α-primase was sufficiently stabilized on carbon film to yield a bi-lobed shape with the two lobes ~120 Å apart (**Figure 6a**). This architecture is essentially the same as a previous negative-stain EM study, in which one lobe is assigned to the catalytic NTD of Pol1 (Pol1-NTD) and the other lobe to the CTD of Pol1, plus the B-subunit and the L- and S-subunits of the primase (Nunez-Ramirez et al., 2011). Cryo-EM of $Ctf4_3$ alone produced 2D class averages that are consistent with the crystal structure (**Figure 6b**). Cryo-EM 2D class averages of a 1:1 molar ratio mixture of $Ctf4_3$ and Pol α-primase yielded a structure comprised of $Ctf4_3$ bound to one catalytic Pol1-NTD of Pol α-primase (**Figure 6c, Figure 6 – figure supplement 1, Table 2**). Increasing the Pol α:$Ctf4_3$ ratio to 3:1 did not change the 1:1 binding with $Ctf4_3$ (**Figure 6 - figure supplement 2**). The presence of the Pol lobe, but absence of the primase lobe in the 2D class averages is consistent with previous studies showing a high degree of flexibility between the primase and polymerase lobes (Baranovskiy and Tahirov, 2017; Nunez-Ramirez et al., 2011; Perera et al., 2013). The 2D averages reveal two contacts between $Ctf4_3$ and Pol1-NTD, but only one of the two contacts is visible in the 3D map (**Figure 6c-d**). These interactions must be weak and flexible, with one contact becoming averaged out in 3D reconstructions, and accounting for the low 12-Å resolution of the 3D map.

The crystal structures of $Ctf4_3$ and Pol1-NTD complexed with a primed DNA-dNTP fit well as two separate rigid-bodies in the upper and lower densities of the $Ctf4_3$–apo Pol1-NTD 3D map, respectively. The docking suggests that the primer-template duplex exits the Pol1-NTD from the bottom face (**Figure 6d, Figure 6 – figure supplement 1**). We added a three-fold excess of Pol α-primase to $Ctf4_3$, but did not observe more than one molecule of Pol α-primase bound to the Ctf4 trimer (**Figure 6 – figure supplement 2**), consistent with the previous observations (Simon et al., 2014). The Pol1-NTD occupies most of the bottom C-face of $Ctf4_3$ (**Figure 6d, Figure 6 – figure supplement 1**), appearing to sterically occlude additional molecules of Pol α-primase and thus explaining the single Pol α-primase-to-$Ctf4_3$ stoichiometry. Notably, in a factory complex with two tightly bound CMGs, there would still remain a vacant CIP site in $Ctf4_3$ for binding of dynamic partner proteins, such as Pol α-primase and other CIP factors (see Discussion).

Reconstitution and characterization of a 2CMG-$Ctf4_3$-1Pol α-primase complex. To investigate complex formation among CMG, $Ctf4_3$ and DNA polymerases, we analyzed by densitometry the sedimentation analyses of a mixture of CMG+$Ctf4_3$ with DNA Pol α-primase and Pol ε. This protein mixture produced a large super-complex that surpassed the size of CMG-$Ctf4_3$ and the Pol ε-CMGE complexes (**Figure 1 – figure supplement 1**). Interestingly, the bulk of excess $Ctf4_3$ is excluded from the large complex suggesting some type of cooperative assembly. Gel scans indicate a stoichiometry of two CMG-Pol ε, one $Ctf4_3$, one Pol α-primase (**Figure 7 – figure supplement 1**), although we can't exclude a possible mixture of complexes. Upon mixing CMG+$Ctf4_3$+Pol α-primase we observed a 2CMG-1$Ctf4_3$-1Pol α-primase complex by negative stain EM (**Figure 7 – figure supplement 2**).

We investigated cooperativity of CMG and Pol α-primase binding to Ctf4 by pull-down assays (**Figure 7a**). Pull-down assays using immobilized $Ctf4_3$ showed an 8-fold increase of Pol α-primase retained on $Ctf4_3$ when CMG was present, and conversely, more CMG bound to $Ctf4_3$ when Pol α-primase was

present, suggesting cooperativity (**Figure 7a**). Cooperativity is consistent with densitometry of CMG-Pol ε-1Ctf4$_3$-1Pol α-primase isolated in a glycerol gradient which excludes most of the Ctf4 trimer (**Figure 7 – figure supplement 1**). Negative stain EM also shows a 2CMG-Ctf4$_3$-1Pol α-primase complex (**Figure 7 – figure supplement 2**). The spontaneous and cooperative assembly of this complex in vitro suggests that the complex may also form in cells and possibly underlies the observations that sister replisomes are held together in cells (Chagin et al., 2016; Saner et al., 2013).

To determine if multimers of CMG bound to Ctf4 retain activity, and thus could operate on two forks at the same time, we performed helicase and replication assays comparing CMG with 2CMG + 1Ctf4$_3$ (preincubated to form 2CMG-Ctf4$_3$ complex as in **Figure 2**) (**Figure 7b-d**). Many reports utilize ATPγS in a preincubation to enable CMG binding the DNA, and preincubation assays indicated that a 10 min preincubation at 30°C with ATPγS was sufficient for CMG to bind the short DNA for helicase assays (**Figure 7 – figure supplement 3)**. Helicase activity was initiated after the 10-min preincubation by adding 5 mM ATP. The results demonstrate that 2CMG-Ctf4$_3$ retains essentially the same helicase activity compared to CMG alone (**Figure 7c**), confirming that CMG retained helicase activity while multimerized by Ctf4$_3$. We also tested other ratios of CMG to Ctf4$_3$ that lack the preincubation step, and may measure binding and unwinding; the same activity was observed using CMG alone or multimerized onto Ctf4$_3$ (**Figure 7 – figure supplement 3**).

We tested the effect of preincubation with ATPγS for replication activity on a ^{32}P-primer forked DNA, which when compared to the helicase substrate has a much longer 3' ssDNA tail, a primer duplex region, and Pol α-primase in the preincubation (**Figure 7 – figure supplement 4**). The results indicate a preincubation of 30 min with ATPγS for the primed replication fork. Thus, for replication assays we used a 30-min preincubation with ATPγS prior to adding dNTPs and 5mM ATP (**Figure 7d**). Comparison of CMG+Pol α-primase vs 2CMG+Ctf4$_3$+Pol α-primase showed that CMG retained full replication activity while multimerized by Ctf4$_3$, again indicating that CMGs multimerized by Ctf4$_3$ are functional. In further support of these results, DNA replication assays of pre-formed isolated CMG-Ctf4$_3$ complexes, preincubated for 2 min with 0.1 mM ATP (beneath the threshold of unwinding, see **Figure 7b**), show that when equal amounts of Ctf4$_3$ in the various CMG-Ctf4 complexes are added to replication assays, the 1.7CMG-Ctf4$_3$ gives about twice the activity of 1CMG-Ctf4$_3$, most simply explained by the presence of the extra CMG in 1.7CMG-Ctf4$_3$ vs 1CMG-Ctf4$_3$ (**Figure 7 – figure supplement 4**). Therefore, CMG helicases are active in replication when multimerized by Ctf4$_3$.

Atomic model for a replication factory. In light of cell-based studies that observe that sister replisomes generated from a bidirectional origin are physically coupled such that the two sister duplexes extrude together away from a point source (Chagin et al., 2016; Saner et al., 2013; Natsume and Tanaka, 2010), and on the basis of our cryo-EM and biochemical analysis, we propose that the observed factory in cells is explained by one Ctf4$_3$ that coordinates two CMGs and one Pol α-primase to form a 2CMG–1Ctf4$_3$–1Pol α-primase core replisome factory. While we observed this core replisome factory in negative stain EM (**Figure 7 – figure supplement 2**), we were unable to reconstruct the full 2CMG-Ctf4$_3$-Pol α-primase by cryo-EM analysis, and therefore we obtained an atomic model for this super-complex factory by superimposing the shared Ctf4$_3$ in the atomic model of 2CMG–Ctf4$_3$ with that of Pol α-Ctf4$_3$ (**Figure 8a-b, Figure 8 – figure supplement 1, Video 3**). The model indicates a factory complex that contains two CMGs on the sides of the Ctf4 disk, and one Pol α-primase on the C-face of the Ctf4 disk. The protein complex consisting of 26 visually observed polypeptides in this >2 MDa factory model give no steric clash among them. This model may explain why Ctf4 has evolved to assemble a trimer, not a dimer, in order to tightly coordinate two CMG helicases, leaving one Ctf4 protomer to bind transient CIP factors such as Pol α-primase. Such a structure, operating at a level

above the individual replisome, may represent the functional unit of a cellular replicon core factory derived from one bidirectional origin as implicated by cellular and microscopy studies (Chagin et al., 2016; Saner et al., 2013). Our dimeric CMG replication factory model suggests possible coordination of the two forks that arise from an origin of replication. As the sister forks grow, the duplicated leading and lagging strands would form loops that push the nascent sister DNAs out from the factory surface a scenario that resembles the proposed replication factory model based on cellular studies (summarized in **Figure 8 – figure supplement 2**) (Chagin et al., 2016; Saner et al., 2013).

Discussion

The factors that mediate the association of different replisomes and how a replication factory looks like have been unknown. The cryo-EM and biochemical studies presented here suggest a higher order architecture of the replication machinery beyond an individual replisome and propose that Ctf4 has evolved as a trimer to simultaneously organize two CMGs and one Pol α-primase by forming a 2CMG-$Ctf4_3$–1Pol α-primase factory. Our factory model conceptually advances on the previous view in which $Ctf4_3$ binds a single CMG of an individual replisome (**Figure 1a**) (Simon et al., 2014; Villa et al., 2016). However, we note that individual replisomes with 1CMG-$Ctf4_3$ and replisome factories with 2CMG-$Ctf4_3$ are not mutually exclusive and that until the factory is confirmed to operate inside the cell, the conclusions drawn here should be regarded as preliminary.

1. Mechanism of bidirectional replication by a replication factory. A factory complex containing a stable 2CMG-$Ctf4_3$ is consistent with cell-based studies and light microscopy of replicating DNA in *S. cerevisiae* cells (Conti et al., 2007; Falaschi, 2000; Kitamura et al., 2006; Ligasova et al., 2009; Natsume and Tanaka, 2010), where sister replication forks are shown by super resolution confocal microscopy with fluorescent markers on DNA to be physically associated within a twin fork replication factory at bidirectional origins and that the daughter duplexes are extruded together from a common protein platform (Kitamura et al., 2006; Saner et al., 2013). The model is also consistent with super resolution microscopy of mammalian replication nuclear foci revealing they are comprised of several single replication factories, each of which represents one bidirectional origin replicon (Chagin et al., 2016).

In the 2CMG factory model (**Figure 8**), the two helicases stand sideways above the $Ctf4_3$ disk, with their respective N-tier rings of the two Mcm2-7 hexamers facing appromiately 120° to each other. Previous studies show that the leading strand enters the N-tier of CMG and proceeds through the central channel of CMG to engage the leading strand Pol ε located at the C-tier of CMG (Georgescu et al., 2017; Goswami et al., 2018). Therefore, at the core of the replication factory, the two parental duplexes enter their respective CMGs at the N-tier where each duplex is unwound by steric exclusion (Fu et al., 2011; Georgescu et al., 2017; Langston and O'Donnell, 2017; Goswami et al., 2018; Kose et al., 2019). In the core replication factory model, two parental duplexes can easily be engaged at the N-tiers of each CMG due to their 120° orientation, and the lagging strand is deflected off the top of the N-tier ring after embrace of the parental duplex by the zinc fingers that encircle dsDNA (Georgescu et al., 2017; Li and O'Donnell, 2018; O'Donnell and Li, 2018; Goswami et al., 2018). Therefore, the unwound leading strands travel through the horizontal central channels of CMGs to exit the left and right sides of the replication factory at their respective CMG C-tier to which the leading Pol ε binds.

2. Pol α-primase is flexibly associated in the replisome. Given the high degree of flexibility between the Pol and primase lobes of Pol α-primase, it seems likely that only one lobe or the other will be observed in the EM depending on which lobe is more "fixed" in place. In an earlier study that contained CMG-Pol ε-Ctf4-Pol α-primase-forked DNA, a density from Pol α-primase was observed at the N-tier of the Mcm ring (Sun et al., 2015). Given that the p48/p58 primase subunits interact with Mcm3, Mcm4,

and Mcm6 (You et al., 2013), the Pol α-primase density was most likely the primase lobe. Pol 1 of Pol α-primase binds directly to $Ctf4_3$ (Simon et al., 2014), and in the present study the Ctf4-Pol α-primase structure is solved in the absence of CMG and DNA. Therefore it is the the Pol1 lobe instead of the primase lobe that is stabilized on Ctf4. Thus, the current study and the earlier study are compatible, but observe different lobes of Pol α-primase. At the time of the earlier work (Sun et al., 2015), the dimeric replisome images were observed but discarded, because we did not know how to interpret those images.

3. Either one or more Pol α-primases may prime the two lagging strands of the coupled sister forks. The lagging strands displaced off the N-tier rings of their respective Mcm2-7 hexamers are near the center between the two CMGs. Such lagging strand positioning allows for and raises the possibility that the single Pol α-primase may prime both lagging strands. The catalytic Pol1 NTD of Pol α-primase binds to the bottom C-face of the $Ctf4_3$ disk (**Figures 6d, Figure 6 – figure supplement 1**). The primase lobe is not visible in the 3D map of $Ctf4_3$–Pol α-primase of this report, but the Pol1-NTD lobe and primase lobe of the bi-lobed Pol α-primase are known to be separated by a distance of ~120 Å and connected via a flexible tether that provides a 70° range of motion between the primase and polymerase lobes, sufficiently long to contact both CMGs in the factory (**Figure 8, and Figure 8 - figure supplement 1)** (Baranovskiy and Tahirov, 2017; Nunez-Ramirez et al., 2011; Perera et al., 2013). Because the primase functions upstream of the Pol 1 subunit of Pol α, and binds the Mcms (You et al., 2013), it is likely that the primase lobe extends upwards passing the 45-Å–thick $Ctf4_3$ disc to reach past the N-face of $Ctf4_3$, placing the primase between the two N-tier rings of the helicases where the two lagging strands are first produced (**Figures 1b and 8a, b**). Therefore, the primase subunits can come in contact with and thereby prime both lagging strands.

However, we do not expect that only one Pol α-primase molecule functions for both lagging strands in a replication factory for several reasons. First, Pol α-primase is fully competent to prime the lagging strand in the absence of Ctf4 in vitro using pure proteins, and is dependent on CMG not Ctf4 for function (Georgescu et al., 2015b; Yeeles et al., 2015; Yeeles et al., 2017), indicating that Ctf4 is not required for replication fork operations per se. Second, the dynamic binding of Pol α-primase to Ctf4 in the dynamic Ctf4 hub view (Villa et al., 2016), especially given the weak binding of the Pol 1 CIP peptide, would only enable a single Pol α-primase to stay bound to Ctf4 for a few seconds or less. Therefore even individual replisomes containing Ctf4 would utilize numerous Pol α-primase binding events over the time needed to repeatedly prime one lagging strand during replisome progression.

4. Multiple CIP factors may still access Ctf4 in the replisome factory. The currently identified CIP factors include Pol α-primase, CMG, Chl1, Dpb2, Tof2, and Dna2; the Pol α-primase, CMG, Dna2, and Chl1 bind the same consensus CIP site of Ctf4, whereas Tof2 and Dpb2 bind a distinct site on Ctf4 (Samora et al., 2016; Villa et al., 2016). The ability of $Ctf4_3$ to bind several different factors is proposed to depend on time-sharing due to weak CIP peptide binding with rapid on/off rates to Ctf4, similar to PCNA binding factors via a conserved PIP (PCNA Interaction Peptide) motif, reviewed in (Georgescu et al., 2015a). Given the tight interaction of 2 CMGs to $Ctf4_3$, we envision three different pathways for CIP proteins to bind $Ctf4_3$ in a replication factory. The first, and simplest, is that the transient binding of Pol α-primase will often vacate one Ctf4 subunit, making it available for other CIP proteins. Indeed, given Pol α-primase still functions in vitro without Ctf4 (Georgescu et al., 2015b; Yeeles et al., 2015; Yeeles et al., 2017), this particular CIP site may often be available for other CIP factors to bind. Second, the Chl1 helicase and Dna2 nuclease are required under particular cellular conditions, during which the replisome may change composition, and this has precedence in the rapid and dynamic rearrangements of proteins in the *E. coli* replisome (Indiani et al., 2009; Lewis et al., 2017). Third, the structures of this report show that the CIP peptide of CMG (in Sld5) is located across a wide gap between CMG and Ctf4,

and the CIP sequence only contacts Ctf4 at the end of a long flexible linker in Sld5. The K_d of the Sld5 CIP peptide to Ctf4 is only 5 μM and can even be deleted without preventing CMG-Ctf4 interaction in living cells (Simon et al., 2014). Given the flexible loop that mediates the Sld5 CIP peptide in the CMG-Ctf4 complex, the Sld5 CIP peptide likely retains the rapid k_{off} implied by the 5 μM K_d and thus can be expected to vacate the Ctf4 CIP site frequently (i.e. milliseconds). While speculative, it is also possible the Sld5 CIP peptide within CMG may be regulated by other proteins, or that other CIP factors that have additional contacts to Ctf4 that can outcompete the weakly bound Sld5 CIP peptide.

5. Independent replisomes and the twin CMG factory model are not mutually exclusive. The current report demonstrates that two (or three) CMG can bind Ctf4 tightly, that CMGs bound to the Ctf4 trimer retain activity, and that a complex of 2(CMG-Pol ε)-1Ctf4$_3$-1Pol α-primase spontaneously assembles in vitro. In vitro single molecule studies in *S. cerevisiae* extracts and *Xenopus* extracts demonstrate that individual replisomes can move apart in opposite directions from an origin and contain only one CMG apiece (Duzdevich et al., 2015; Yardimci et al., 2010). While these experiments reveal that replisomes can act individually, these experiments utilize DNA tethered at both ends and thus DNA looping needed in our factory model would not be observed. Thus if factories were present, only when they dissociate to form independent forks would replication forks on doubly tethered DNA be visualized. Alternatively, Xenopus egg extracts may be programmed to replicate a bit differently from normal cells. It is worth noting that neither the model of an individual replisome nor the model of a dimeric replisome factory have been proven to exist inside cells. Because the same proteins are present in both models, they may not be mutually exclusive and may both exist in cells. If true, the different models may even fulfill distict functions. Clearly, cellular studies are needed to untangle these scenarios.

6. Implications of a replisome factory on nucleosome distribution. During replication the epigenetic marks on nucleosomes are distributed nearly equally to the two daughter duplexes (Gan et al, 2018; Petryk et al., 2018; Yu et al., 2018). The general view is that the H3H4 tetramer, which carries the bulk of epigenetic marks, binds DNA tightly and is transferred to nascent DNA independent of H2AH2B dimers that are easily displaced and exchanged (Alabert et al., 2017). Two binding sites for H3H4 exist in the replisome: The N-terminal region of Mcm2 binds H3H4 (Huang et al., 2015; Richet et al., 2015), and the Dpb3/4 subunits of Pol ε bind H3H4 at the C-face of CMG (Bellelli et al., 2018; Tackett et al., 2005; Sun et al, 2015). Recent studies have found specific roles of these H3H4 sites in transfer of parental histones to daughter DNAs during replication (Gan et al., 2018; Petryk, et al., 2018; Yu et al., 2018; Evrin. et al., 2018). Moreover, the N-terminal region of Pol 1 (i.e. the DNA Pol of Pol α-primase) binds H2A/H2B, and mutations in either Pol 1, Mcm2 or Ctf4 have a negative effect on transfer of parental histone marks to the lagging strand duplex (Evrin et al., 2018; Gan et al., 2018). Hence Mcm2-Ctf4-Pol α forms an "axis" for nucleosome transfer from parental DNA to the lagging daughter DNA (Gan et al., 2018). If only one Pol α-primase exists for two replication forks as in our 2CMG-Ctf4 factory model, during the time for transfer of a parental H3H4 to the lagging strand of one fork, the other fork in the opposite CMG would have progressed the same distance for transfer of another parental H3H4 to the leading strand. In this view, the architecture of our factory model facilitates the observed equal transfer of histones to both leading and lagging strand products (Gan et al, 2018; Petryk et al., 2018; Yu et al., 2018).

There is another aspect of the replisome factory architecture that may play a role in the proposed Mcm2-Ctf4-Pol α axis of nucleosome distribution. Two Mcm2's are needed to bind one H3H4 tetramer (Huang et al., 2015; Richet, et al., 2015). In our structure, Mcm2 is ordered from Pro-201, and there is a 200 residue long peptide that is intrinsically disordered. So the H3H4 binding site (residues 61-130) is within this unstructured peptide. In our factory model, the two Mcm2's, one from each CMG helicase, may project out a pair of long tentacles (Mcm2 residues 1-200) between the two CMGs, and the two tentacles

403 would conspire to capture one H3H4 to allow the "Mcm-Ctf4-Pol α "axis" to participate in equal
404 deposition of parental histone marks on both strands of wt cells, much like the single Pol α-primase in
405 the factory. An alternative to the use of two Mcm2's is that the H3H4 tetramer could be split so that one
406 H3H4 dimer is bound by one Mcm2 and one Asf1 (Huang et al., 2015; Richet et al., 2015, add Wang et
407 al Protein and cell 2015, 693-7). However, mass spectrometry studies indicate that the H3H4 tetramer
408 remains intact during replication (Xu et al., 2010).
409
410 Interestingly, Okazaki fragments are sized relative to the nucleosome repeat (Smith and Whitehouse,
411 2012). If nucleosome transfer is coordinated with Okazaki fragment synthesis, the parental nucleosome
412 will occupy approximately the same sequence on the nascent DNA as it did on the parental DNA, as
413 observed experimentally (Madamba et al., 2017). To conclude, the current study is only the beginning of
414 a comprehensive understanding of how replication is organized in the cell. We expect that additional
415 proteins, further layers of organization, and yet to be determined dynamics exist in nuclear replication
416 factories. The replisome architecture and actions in the context of chromatin and epigenetic inheritance
417 are important areas for future research.
418
419

METHODS

Reagents. Radioactive nucleotides were from Perkin Elmer and unlabeled nucleotides were from GE Health-care. Protein concentrations were determined using the Bio-Rad Bradford Protein stain using BSA as a standard. Purification of *S. cerevisiae* Pol α-primase, Pol ε, CMG, the C-terminal half of Ctf4 (residues 471-927), and full length Ctf4 were purified according to previously published procedures (Georgescu et al., 2014; Langston et al., 2014). The C-terminal half of Ctf4 is necessary and sufficient for Ctf4 binding to CMG and Pol α-primase , as shown previously (Simon et al., 2014). Oligonucleotides were from ITG (Integrated DNA Technologies). ATPγS used for experiments in this report were purchased from Roche (catalog 11162306001).

EM sample preparation of CMG-Ctf4$_3$ complexes. CMG (3.36 nmol) was mixed with Ctf4$_3$ (1.7 nmol) in a final volume of 1.37 ml of buffer A (20 mM Tris-acetate (pH 7.6), 1 mM DTT, 2 mM magnesium acetate) plus 200 mM KCl. The mixture was incubated on ice for 30 min, then injected onto a 0.25 ml MonoQ column equilibrated in buffer A + 200 mM KCl. The column was eluted with a 20-column linear gradient of buffer A + 200 mM KCl to buffer A + 600 mM KCl. Fractions of 0.25 ml were collected and protein concentration was determined using the Bio-Rad Bradford Protein stain and BSA as a standard. Fractions were analyzed in a Commasie stained 8% SDS-polyacrylamide gel and gel lanes were scanned using a Typhoon 9400 laser imager (GE Healthcare). Scanned gels were analyzed using ImageQuant TL v2005 software and the two peak fractions were pooled and concentrated to 8.5 mg/ml in 79 µl. The sample was mixed with a 4-fold excess of a DNA 20-mer (5'-Cy3-dTdT$_{biotin}$dT$_{18}$) oligonucleotide, 0.2 mM AMPPNP (final) which binds CMG. The sample was incubated 2 h on ice then applied onto a Superose 6 Increase 3.2/300 gel filtration column (GE Healthcare) equilibrated in 20 mM Tris-acetate (pH 7.5), 1 mM DTT, 2 mM magnesium acetate, 60 mM potassium glutamate, 0.1 mM AMPPNP. The Cy3 DNA was added to visualize elution of CMG-Ctf4 at 565 nm, along with monitoring elution at 280 nM. Fractions were analyzed by SDS-PAGE and scanned on a Typhoon 9400 laser imager (GE Healthcare) to estimate the stoichiometry of CMG-to-Ctf4 in each fraction. The samples used for analysis were fraction 37 (0.35 mg/ml), fraction 35 (0.48 mg/ml), fraction 33 (0.42 mg/ml) and fraction 31 (0.35 mg/ml).

Cryo-EM of Ctf4$_3$, Ctf4$_3$–Pol α-primase and Ctf4$_3$–CMG complexes. To prepare cryo-EM grids, individual fractions of CMG-Ctf4$_3$ from the gel filtration column were dialyzed against buffer A and concentrated to 0.35-0.48 mg/ml. Then 3 µl aliquots were applied to glow-discharged C-flat 1.2/1.3 holey carbon grids, incubated for 10 seconds at 6 °C and 95% humidity, blotted for 3 s then plunged into liquid ethane using an FEI Vitrobot IV. In C-flat R1.2/1.3 holey carbon film grids, the CMG-Ctf4$_3$ particles distributed well for each of the samples. The Ctf4$_3$–CMG grids were loaded into an FEI Titan Krios electron microscope operated at a high tension of 300 kV and images were collected semi-automatically with EPU under low-dose mode at a nominal magnification of ×130,000 and a pixel size of 1.074 Å per pixel. A Gatan K2 summit direct electron detector was used under super-resolution mode for image recording with an under-focus ranging from 1.5 to 2.5 µm. A Bioquantum energy filter installed in front of the K2 detector was operated in the zero-energy-loss mode with an energy slit width of 20 eV. The dose rate was 10 electrons per Å^2 per second and total exposure time was 6 s. The total dose was divided into a 30-frame movie so each frame was exposed for 0.2 s. Approximately 5,900 raw movie micrographs were collected.

Analysis of Ctf4$_3$ used a sample of Ctf4$_3$ at 1.8 mg/ml in 20 mM Tris-acetate (pH 7.5), 1 mM DTT, 2 mM magnesium acetate, 60 mM potassium glutamate. For the Pol α-primase-Ctf4 EM analysis we were unable to isolate a complex between these weak interacting components. Hence, we directly mixed the proteins for EM analysis. The samples contained Ctf4$_3$ and Polα-primase complex either at 1:1 molar

ratio at a final concentration of 2.25 mg/ml, or at 1:3 molar ratio at a final concentration of 1.75 mg/ml, in 20 mM Tris-Acetate pH 7.5, 0.5 mM EDTA, 100 mM KGlutamate and incubated 20 minutes on ice. The samples were then applied to grids and plunge fronzen as described above. We collected ~1000 raw movie micrographs for each sample on an FEI Talos Arctica operated at 200 kV with a Falcon III direct electron detector. Data was collected semi-automatically with EPU at a nominal magnification of ×120,000 and pixel size of 1.21 Å per pixel. The under-focus value ranged from 1.5 to 2.5 μm. The dose rate was 20 eV per $Å^2$ per second and total exposure time was 3 s. The total dose was divided into a 39-frame movie so each frame was exposed for 0.07 s.

Negative-staining EM of Pol α-primase. A sample of 2 μL of yeast Pol α-primase at 0.1 mg/mL in 20 mM Tris-Acetate pH 7.5, 0.5 mM EDTA, 100 mM KGlutamate was applied to a glow-discharged carbon-coated copper grid for 30 s. Excess sample was blotted away using Whatman filter paper (Grade 1) with subsequent application of 2 μL of a 2% (w/v) aqueous solution of uranyl acetate. The staining solution was left on the grid for 30 s before the excess was blotted away. The staining solution was applied for a second time, blotted away and left to dry for 15 min before EM. A total of 50 micrographs were collected on a 2k by 2k CCD camera in FEI Tecnai G2 Spirit BioTWIN TEM operated at 120 kV at a magnification of ×30,000, corresponding to 2.14 Å per pixel at the sample level. Electron micrographs were processed using Relion 2 (Scheres, 2012). After CTF estimation and correction using Gctf (Zhang, 2016), particles in each micrograph were automatically picked using a Gaussian blob as the template at a threshold of 0.1, leading to a dataset of 24,712 raw particles. 2D classification was run for 25 iterations with the class number assigned to 100, the particle mask diameter set to 256 Å, the regularization parameter T left at the default value of 2, and the maximum number of significant coarse weights restricted to 500.

For observing the CMG-$Ctf4_3$-Pol α-primase complex, a sample of 2 μL of the ternary mixture at 0.12 mg/ml was applied to a glow-discharged carbon-coated grid for 1 min, then a 2 μL drop of 2% (w/v) aqueous solution of uranyl acetate was applied to the grid for and addtional 1 min, then blotted away with a piece of filter paper, and the staining step was repeated one more time. The dried EM grid was loaded onto an 120 kV FEI Tecnai G2 Spirit EM with a 2K × 2K CCD camera. A total of 200 micrographs were collected at a magnification of ×30,000, corresponding to 2.14 Å per pixel. After CTF estimation and correction using CTFFIND4, particles were manually picked in Relion 2.1. About 9,000 particles were picked for 2D classification. Several 2D averages showed a binary complex of CMG-$Ctf4_3$, and the ternary complex of CMG-$Ctf4_3$ - Pol α-primase complex.

Image processing and 3D reconstruction. The movie frames were first aligned and superimposed by the program Motioncorr 2.0 (Zheng et al., 2017). Contrast transfer function parameters of each aligned micrograph were calculated using the program CTFFIND4 (Rohou and Grigorieff, 2015). All the remaining steps, including particle auto selection, 2D classification, 3D classification, 3D refinement, and density map post-processing were performed using Relion-2.1 (Scheres, 2012). For the 1CMG–$Ctf4_3$ sample, templates for automatic picking were generated from 2D averages calculated from about ~10,000 manually picked particles in different views. Automatic particle selection was then performed for the entire data set, and 759,267 particles were picked. Selected particles were carefully inspected; "bad" particles were removed, some initially missed "good" particles were re-picked, and the remaining good particles were sorted by similarity to the 2D references, in which the bottom 10% of particles with the lowest z-scores were removed from the particle pool. 2D classification of all good particles was performed and particles in the classes with unrecognizable features by visual inspection were removed. A total of 564,011 particles were then divided into two groups containing either a single CMG or two or three copies of CMG for further 3D classification. For 3D reconstruction of the various $Ctf4_3$-CMG complexes, the low pass-filtered CMG-apo structure was used as the starting model, leading

to the first 3D map of the $Ctf4_3$-$(CMG)_3$ complex. We then used Chimera to mask out either one or two CMG densities from the 3D map of $Ctf4_3$-$(CMG)_3$ to generate a starting model for 1CMG-$Ctf4_3$ and 2CMG-$Ctf4_3$ respectively. Four 3D models were derived from each group, and models that appeared similar were combined for final refinement. The models not chosen were distorted and those particles were discarded. The final three datasets that contain single CMG ($Ctf4_3$–CMG_1), two CMGs ($Ctf4_3$–CMG_2), and three CMGs ($Ctf4_3$–CMG_3) were used for final 3D refinement, resulting in three 3D density maps at 3.9 Å, 5.8 Å and 7.0 Å resolution, respectively. The resolution was estimated by the gold-standard Fourier shell correlation, at the correlation cutoff value of 0.143. The 3D density map was sharpened by applying a negative B-factor of −146, −135 and −143 $Å^2$, respectively. Local resolution was estimated using ResMap. In the 1CMG-$Ctf4_3$ analysis, the density of the Mcm2-7 CTD motor region was weak and noisy. A mask was used to exclude the CTD ring, and the remaining region composed of $Ctf4_3$–Cdc45–GINS–Mcm2-7 N-tier ring had an estimated resolution of 3.8 Å, based on the gold standard Fourier shell correlation curve.

For the $Ctf4_3$–Polα-primase dataset, ~5,000 particles in different views were manually picked to generate the templates. Automatic particle selection was then performed for the entire dataset, and 237,688 particles were initially picked in Relion-2.1. Similar to the image process in $Ctf4_3$–CMG, "bad" and structurally heterogeneous particles were removed by visual inspection. After 2D classification, 142,806 particles in many different views were selected for further 3D classification. The selected particles were separated into 5 classes by the 3D classification procedure, using a low-pass filtered Ctf4 trimer structure as the starting model. Two good classes were selected and combined for final 3D refinement. The final 3D refinement produced a 12-Å 3D density map. The resolution of the map was estimated by the gold-standard Fourier shell correlation, at the correlation cutoff value of 0.143. The 3D density map was sharpened by applying a negative B-factor of −162 $Å^2$.

For the $Ctf4_3$ dataset, we picked about 3,000 particles in different views to generate the templates. Automatic particle picking was performed for the entire dataset containing abut 500 micrographs, and 113,936 particles were picked in Relion-2.1; then 2D classification was performed to produce a set of well-defined 2D averages. 3D classification and 3D reconstruction were not performed because the crystal structure of $Ctf4_3$ is available and our purpose was only to obtain the cryo-EM 2D averages.

Atomic modeling, refinement, and validation. The modeling of $Ctf4_3$–CMG_1, $Ctf4_3$–CMG_2 and $Ctf4_3$–CMG_3 was based on the structure of CMG (PDB 3JC5) and $Ctf4_3$ (PDB 4C8H). For $Ctf4_3$–CMG_1, one CMG and one Ctf4 trimer were directly docked as rigid bodies into the EM map using Chimera (Pettersen et al., 2004). The initial modeling was followed by further manual adjustments using COOT (Emsley et al., 2010), guided by residues with bulky side chains like Arg, Phe, Tyr and Trp. The improved model was then refined in real space against the EM densities using the phenix.real_space_refine module in PHENIX (Adams et al., 2010). For $Ctf4_3$–CMG_2 and $Ctf4_3$–CMG_3, Chimera was used to rigid-body dock two or three copies of CMG and one $Ctf4_3$ into the corresponding EM map. Due to the low resolution of the latter two maps, the atomic models were not subject to further refinement. Finally, the quality of the refined atomic model of $Ctf4_3$–CMG was examined using MolProbity (Chen et al., 2010). For modeling of the $Ctf4_3$–Polα-primase 3D map, one Ctf4 trimer (PDB 4C8H) and one Polα-primase catalytic NTD (PDB 4FYD) were docked as two separate rigid bodies into the 3D map in Chimera. Due to the low resolution of 3D map, the model was neither manually adjusted nor subjected to refinement. Structural figures were prepared in Chimera and Pymol (https://www.pymol.org).

Glycerol gradient sedimentation. To examine complex formation, 0.12 nmol of CMG was mixed with 0.12 nmol $Ctf4_3$, 0.12 nmol of Pol ε and 0.12 nmol Pol α-primase in 150 µl of 20 mM Tris-acetate (pH 7.6), 1 mM DTT, 2 mM Mg-OAc, 100 mM NaCl (final) for 30 min at 16 °C, and the mixture was layered on top of an 11.2 mL 15–35% (vol/vol) glycerol gradient in 20 mM Tris-acetate (pH 7.6), 1 mM DTT, 2 mM magnesium acetate, 50 mM NaCl and spun at 4 °C for 16 h in a Sorvall 90SE ultracentrifuge using a T-865 rotor. Five drop fractions were collected from the bottom of the centrifuge tubes, and 20 µL samples were analyzed by SDS/PAGE stained with Coomassie Blue. Similar gradient analyses were performed for submixtures of the proteins. A parallel gradient was also performed using protein standards (BioRad 151–1901) in the same buffer. Gels were scanned and quantitated using Image J software and relative moles of protein in each band were calculated, taking into account their native mw. Only subunits the size of Cdc45 or larger were analyzed, as smaller subunit bands were too light for analysis. The full-length $Ctf4_3$ was used to enhance its staining capacity, as the small C-half of $Ctf4_3$ was not well distinguished above background. The full-length $Ctf4_3$ overlapped with Mcm4 and required taking the overlap into account (see legend to **Figure 7 – figure supplement 1**).

Pull-down assays. Pull-down assays were performed by mixing 20 pmol of N-terminal labeled streptag-Ctf4 trimer with 60 pmol Pol α-primase (when present) and 60 pmol CMG (when present) at 25°C for 10 min. Then the volume of the protein solution was adjusted to 50 µl with binding buffer (20 mM Tris-Acetate, pH 7.5, 1 mM DTT, 5% glycerol, 2 mM magnesium acetate, 50 mM KGlutamate and 50 mM KCl) before being mixed with 50 µl of a 50% suspension of StrepTactin magnetic beads (Qiagen). The protein-bead mixture was incubated in a Thermomixer at 1250 rpm, 4°C for 1 hr. The beads were then collected with a magnetic separator and the supernatant containing unbound proteins was removed. The beads were washed twice with 100 µl binding buffer and bound proteins were eluted by incubating the beads in 50 µl of the same buffer supplemented with 5 mM biotin at 25°C for 15 min. The eluted proteins were analyzed in an 8% SDS-polyacrylamide gel and scanned and quantitated using a Typhoon 9400 laser imager (GE Healthcare).

Helicase assays: DNA oligos used to form the forked substrate were "lagging helicase oligo": (5'GGCAGGCAGGCAGGCAGGCAGGCAGGCAGGCAGGCAGGCTTGTCCTAGCAAGCCAGAA TTCGGCAGC*G*T*C) and "leading helicase oligo": (5'GACGCTGCCGAATTCTGGCTTGCTAGGACATTTTTTTTTTTTTTTTTTTTTTTTTTTTT TTTT*T*T*T). Asterisks denote thiodiester linkages. The leading helicase oligo was ^{32}P-5' end-labeled and annealed to its respective lagging helicase oligo to form the forked DNA substrate. The forked DNA was isolated from a native PAGE. In the experiments of **Figure 7b**, 2CMG-$Ctf4_3$ complexes were formed by preincubating 276 nM CMG with 138 nM full length $Ctf4_3$ on ice for 15 min. and then 25°C for 10 min. CMG or CMG-Ctf4 complexes were added to reactions to give a final concentration of 24 nM CMG, 0.5 nM forked DNA substrate, and 5mM ATP in a final buffer of 20 mM Tris-Acetate pH 7.6, 5 mM DTT, 0.1 mM EDTA, 10 mM $MgSO_4$, 30 mM KCl. Reactions were preincubated with 0.1 mM ATPγS (Roche) for 10 min at 30°C with DNA and either CMG or CMG-Ctf4 before initiating unwinding upon adding 5mM ATP. Reactions were quenched at the times indicated with 20 mM EDTA and 0.1% SDS (final concentrations), and analyzed on a 10% native PAGE in TBE buffer. The assays of **Figure 7 – figure supplement 3a** (i.e. that tested preincubation time with 0.1 µM ATPγS) were performed as in **Figure 7b**, except reactions were preincubated for different times with ATPγS at 30°C before initiating unwinding with 5mM ATP for 10 min. An aliquot from each preincubation reaction was removed and quenched (for analysis of unwinding during preincubation), and then 5 mM ATP was added to the remainder of the reaction for analysis of unwinding with ATP after the ATPγS preincubation step. All reactions were quenched with 20 mM EDTA/0.1% SDS. Reactions of **Figure 7 – figure supplement 3b** utilized the amounts of $Ctf4_3$ indicated, preincubated with CMG as above to form

the CMG-Ctf4 complex, and DNA unwinding was initiated upon adding either 20 nM CMG, or 20 nM CMG-Ctf4 with 5 mM ATP for 30 min at 30°C. The assays included 50 nM unlabeled LEADING helicase oligo as a trap 2' after adding ATP. Gels were exposed to a phosphor screen then scanned and quantitated on a Typhoon 9400 laser imager (GE Healthcare).

Replication assays. Leading strand replication experiments used a forked DNA substrate formed from the following oligonucleotides: Leading strand template 180mer: 5'AGGTGTAGATTAATGTGGTTAGAATAGGGATGTGGTAGGAAGTGAGAATTGGAGAGTGT GTTTTTTTTTTTTTTTTTTTTTTTTTTTTTTTTTTTTTTTTAAAGGTGAGGGTTGGGAAGTGGA AGGATGGGCTCGAGAGGTTTTTTTTTTTTTTTTTTTTTTTTTTTTTTTTTTT*T*T*T-3', and lagging strand template 100mer: 5'-GGCAGGCAGGCAGGCAGGCAGGCAGGCAGGCAGGCAGGCACACACTCTCCAATT CTCACTTCCTACCACATCCCTATTCTAACCACATTAATCTACA*C*C*T-3' Asterisks are thiodiester linkages. The fork was primed for leading strand DNA replication with 5'-^{32}P-CCTCTCGAGCCCATCCTTCCACTTCCCAACCCTCACC-3'. The 2CMG-Ctf4$_3$ complexes were reconstituted by incubating 276 nM CMG with 138 nM Ctf4$_3$ on ice for 15 min. and then 25°C for 10 min. When present, 276 nM Pol α-primase was also added to the reconstitution reaction to form complexes with an average stoichiometry of 2CMG-Ctf4$_3$-Pol α-primase. For the reactions of **Figure 7c**, reactions contained 20 nM CMG, 20 nM Pol α-primase, 10 nM Ctf4$_3$ (where indicated) and 0.5 nM ^{32}P-primed forked substrate (final concentrations) in a buffer consisting of 25 mM Tris-Acetate pH 7.5, 5% glycerol, 2 mM DTT, 10 mM magnesium sulfate, 1 μM dTTP and preincubated with 100 μM ATPγS for 30 min. DNA synthesis was initiated upon adding 5 mM ATP and 100 μM each dNTP, and stopped at the indicated times using an equal volume of 1% SDS, 40 mM EDTA, 90% formamide. For the preincubation analysis of **Figure 7 – supplemental figure 4a** (top), the same procedure was followed as **Figure 7b**, except the preinubation time varied as indicated, and the replication time was 8 min. Replication reactions in **Figure 7 – figure supplement 4b** were performed similarly except there was no preincubation step and the buffer included 10 μg/ml BSA, 50 mM K glutamate, 0.1 mM EDTA. Reaction products were analyzed on 10% PAGE gels containing 6M urea in TBE buffer, then exposed to a phosphorimager screen and imaged with a Typhoon FLA 9500 (GE Healthcare). Gel bands were quantitated with ImageQuant software.

Acknowlegement. Cryo-EM data were collected at the David Van Andel Advanced Cryo-Electron Microscopy Suite at the Van Andel Research Institute. We thank X. Meng for help with data collection. This study was supported by the US National Institutes of Health R01 grants GM111742 and GM124170 (to H.L.), and GM115809 (to M.E.O), the Van Andel Research Institute (H.L.), and the Howard Hughes Medical Institute (M.E.O).

Accession codes. The 3D cryo-EM maps of Ctf4$_3$–CMG$_1$, Ctf4$_3$–CMG$_2$, and Ctf4$_3$–CMG$_3$ at 3.8-Å, 5.8-Å and 7.0-Å resolution have been deposited in the Electron Microscopy Data Bank under accession codes EMD-20471, EMD-20472 and EMD-20473, respectively. The corresponding atomic models have been deposited in the Protein Data Bank under accession codes PDB 6PTJ, PDB 6PTN, PDB 6PTO, respectively.

REFERENCES

Abe T, Kawasumi R, Giannattasio M, Dusi S, Yoshimoto Y, Miyata K, Umemura K, Hirota K, Branzei D. 2018. AND-1 fork protection function prevents fork resection and is essential for proliferation. *Nat Commun* **9**:3091. DOI: https://doi.org/10.1038/s41467-018-05586-7, PMID: 30082684

Abid Ali F, Renault L, Gannon J, Gahlon HL, Kotecha A, Zhou JC, Rueda D, Costa A. 2016. Cryo-EM structures of the eukaryotic replicative helicase bound to a translocation substrate. *Nat Commun* **7**:10708. DOI: https://doi.org/10.1038/ncomms10708, PMID: 26888060

Adams PD, Afonine PV, Bunkoczi G, Chen VB, Davis IW, Echols N, Headd JJ, Hung LW, Kapral GJ, Grosse-Kunstleve RW, McCoy AJ, Moriarty NW, Oeffner R, Read RJ, Richardson DC, Richardson JS, Terwilliger TC, Zwart PH. 2010. PHENIX: a comprehensive Python-based system for macromolecular structure solution. *Acta Crystallogr D Biol Crystallogr* **66**:213-221. DOI: https://doi.org/10.1107/S0907444909052925, PMID: 20124702

Alabert C, Jasencakova Z, Groth A. 2017. Chromatin Replication and Histone Dynamics.Adv Exp Med Biol. **1042**:311-333. doi: 10.1007/978-981-10-6955-0_15. doi: 10.1007/978-981-10-6955-0_15. PMID: 29357065.

Baranovskiy AG, Tahirov TH. 2017. Elaborated Action of the Human Primosome. *Genes (Basel)* **8**. DOI: https://doi.org/10.3390/genes8020062, PMID: 28208743

Bell SP, Labib K. 2016. Chromosome Duplication in Saccharomyces cerevisiae. *Genetics* **203**:1027-1067. DOI: https://doi.org/10.1534/genetics.115.186452, PMID: 27384026

Bellelli R, Belan O, Pye VE, Clement C, Maslen SL, Skehel JM, Cherepanov P, Almouzni G, BoultonSJ. (2018) POLE3-POLE4 Is a Histone H3-H4 Chaperone that Maintains Chromatin Integrity during DNA Replication. Mol Cell. **72**:112-126. e5. doi: 10.1016/j.molcel.2018.08.043. Epub 2018 Sep 11. PMCID: PMC6179962.

Burgers PMJ, Kunkel TA. 2017. Eukaryotic DNA Replication Fork. *Annu Rev Biochem* **86**:417-438. DOI: https://doi.org/10.1146/annurev-biochem-061516-044709, PMID: 28301743

Burnham DR, Kose HB, Hoyle RB, Yardimci H. (2019) The mechanism of DNA unwinding by the eukaryotic replicative helicase. Nat Commun. **10**:2159. doi: 10.1038/s41467-019-09896-2. PMID 30189141.

Chagin VO, Casas-Delucchi CS, Reinhart M, Schermelleh L, Markaki Y, Maiser A, Bolius JJ, Bensimon A, Fillies M, Domaing P, Rozanov YM, Leonhardt H, Cardoso MC. 2016. 4D Visualization of replication foci in mammalian cells corresponding to individual replicons. *Nat Commun* **7**:11231. DOI: https://doi.org/10.1038/ncomms11231, PMID: 27052570

Chen VB, Arendall WB, 3rd, Headd JJ, Keedy DA, Immormino RM, Kapral GJ, Murray LW, Richardson JS, Richardson DC. 2010. MolProbity: all-atom structure validation for macromolecular crystallography. *Acta Crystallogr D Biol Crystallogr* **66**:12-21. DOI: https://doi.org/10.1107/S0907444909042073, PMID: 20057044

Conti C, Sacca B, Herrick J, Lalou C, Pommier Y, Bensimon A. 2007. Replication fork velocities at adjacent replication origins are coordinately modified during DNA replication in human cells. *Mol Biol Cell* **18**:3059-3067. DOI: https://doi.org/10.1091/mbc.e06-08-0689, PMID: 17522385

Costa A, Ilves I, Tamberg N, Petojevic T, Nogales E, Botchan MR, Berger JM. (2011) The structural basis for MCM2-7 helicase activation by GINS and Cdc45. Nat Struct Mol Biol. **18**:471-7. doi: 10.1038/nsmb.2004. Epub 2011 Mar 6. PMID: 21378962

Douglas ME, Ali FA, Costa A, Diffley JFX. (2018) The mechanism of eukaryotic CMG helicase activation. Nature. **555**:265-268. doi: 10.1038/nature25787. Epub 2018 Feb 28. PMID:29489749

Duzdevich D, Warner MD, Ticau S, Ivica NA, Bell SP, Greene EC. 2015. The dynamics of eukaryotic replication initiation: origin specificity, licensing, and firing at the single-molecule level. *Mol Cell* **58**:483-494. DOI: https://doi.org/10.1016/j.molcel.2015.03.017, PMID: 25921072

Emsley P, Lohkamp B, Scott WG, Cowtan K. 2010. Features and development of Coot. *Acta Crystallogr D Biol Crystallogr* **66**:486-501. DOI: https://doi.org/10.1107/S0907444910007493, PMID: 20383002.

Evrin, C., Maman, J.D., Diamante, A., Pellegrini, L., and Labib, K. (2018) Histone H2A-H2B binding by Pol α in the eukaryotic replisome contributes to the maintenance of repressive chromatin. EMBO J. **37**: e99021, doi: 10.15252/embj.201899021. Epub 2018 Aug 13 PMID:30104407, PMCID: PMC6166128.

Falaschi A. 2000. Eukaryotic DNA replication: a model for a fixed double replisome. *Trends Genet* **16**:88-92. DOI: https://doi.org/10.1016/S0168-9525(99)01917-4, PMID: 10652536

Fu YV, Yardimci H, Long DT, Ho TV, Guainazzi A, Bermudez VP, Hurwitz J, van Oijen A, Scharer OD, Walter JC. 2011. Selective bypass of a lagging strand roadblock by the eukaryotic replicative DNA helicase. *Cell* **146**:931-941. DOI: https://doi.org/10.1016/j.cell.2011.07.045, PMID: 21925316

Gambus A, Jones RC, Sanchez-Diaz A, Kanemaki M, van Deursen F, Edmondson RD, Labib K. 2006. GINS maintains association of Cdc45 with MCM in replisome progression complexes at eukaryotic DNA replication forks. *Nat Cell Biol* **8**:358-366. DOI: https://doi.org/10.1038/ncb1382, PMID: 16531994

Gambus A, van Deursen F, Polychronopoulos D, Foltman M, Jones RC, Edmondson RD, Calzada A, Labib K. 2009. A key role for Ctf4 in coupling the MCM2-7 helicase to DNA polymerase alpha within the eukaryotic replisome. *EMBO J* **28**:2992-3004. DOI: https://doi.org/10.1038/emboj.2009.226, PMID: 19661920

Gan H, Serra-Cardona A, Hua X, Zhou H, Labib K, Yu C, Zhang Z. (2018) The Mcm2-Ctf4-Polα Axis Facilitates Parental Histone H3-H4 Transfer to Lagging Strands. *Mol Cell*. **72**:140-151. doi: 10.1016/j.molcel.2018.09.001. Epub 2018 Sep 20 PMID:30244834

Georgescu R, Langston L, O'Donnell M. 2015a. A proposal: Evolution of PCNA's role as a marker of newly replicated DNA. *DNA Repair (Amst)* **29**:4-15. DOI: https://doi.org/10.1016/j.dnarep.2015.01.015, PMID: 25704660

Georgescu R, Yuan Z, Bai L, de Luna Almeida Santos R, Sun J, Zhang D, Yurieva O, Li H, O'Donnell ME. 2017. Structure of eukaryotic CMG helicase at a replication fork and implications to replisome architecture and origin initiation. *PNAS* **114**:E697-E706. DOI: https://doi.org/10.1073/pnas.1620500114, PMID: 28096349

Georgescu RE, Langston L, Yao NY, Yurieva O, Zhang D, Finkelstein J, Agarwal T, O'Donnell ME. 2014. Mechanism of asymmetric polymerase assembly at the eukaryotic replication fork. *Nat Struct Mol Biol* **21**:664-670. DOI: https://doi.org/10.1038/nsmb.2851, PMID: 24997598

Georgescu RE, Schauer GD, Yao NY, Langston LD, Yurieva O, Zhang D, Finkelstein J, O'Donnell ME. 2015b. Reconstitution of a eukaryotic replisome reveals suppression mechanisms that define leading/lagging strand operation. *Elife* **4**:e04988. DOI: https://doi.org/10.7554/eLife.04988, PMID: 25871847

Gillespie PJ, Blow JJ. 2010. Clusters, factories and domains: The complex structure of S-phase comes into focus. *Cell Cycle* **9**:3218-3226. DOI: https://doi.org/10.7554/eLife.04988, PMID: 25871847

Goren A, Cedar H. 2003. Replicating by the clock. *Nat Rev Mol Cell Biol* **4**:25-32. DOI: https://doi.org/10.1038/nrm1008, PMID: 12511866

Goswami P, Abid Ali F, Douglas ME, Locke J, Purkiss A, Janska A, Eickhoff P, Early A, Nans A, Cheung AMC, Diffley JFX, Costa A. (2018) Structure of DNA-CMG-Pol epsilon elucidates the roles of the non-catalytic polymerase modules in the eukaryotic replisome. Nat Commun. 9:5061. doi: 10.1038/s41467-018-07417-1. PMID: 30498216

He, H., Li, Y., Dong, Q., Chang, A.Y., Gao, F., Chi, Z., Su, M., Zhang, F., Ban, H., Martienssen, R., Chen, Y.H., and Li, F. (2017). Coordinated regulation of heterochromatin inheritance by Dpb3-Dpb4 complex. Proc Natl Acad Sci U S A **114**, 12524-12529. doi: 10.1073/pnas.1712961114. Epub 2017 Nov 6. PMID:29109278, PMCID: PMC5703312.

Iida T, Araki H (2004) Noncompetitive counteractions of DNA polymerase epsilon and ISW2/yCHRAC for epigenetic inheritance of telomere position effect in Saccharomyces cerevisiae. Mol Cell Biol **24**: 217 – 227. DOI:10.1128/mcb.24.1.217-227.2004. PMID:14673157; PMCID: PMC303358.

Huang, H., Strømme, C.B., Saredi, G., Ho¨ dl, M., Strandsby, A., Gonza´lez-Aguilera, C., Chen, S., Groth, A., and Patel, D.J. (2015). A unique binding mode enables MCM2 to chaperone histones H3-H4 at replication forks. Nat. Struct. Mol. Biol. **22**, 618–626. doi: 10.1038/nsmb.3055. Epub 2015 Jul 13. PMID:26167883.

Ilves I, Petojevic T, Pesavento JJ, Botchan MR. 2010. Activation of the MCM2-7 helicase by association with Cdc45 and GINS proteins. *Mol Cell* **37**:247-258. DOI: https://doi.org/10.1016/j.molcel.2009.12.030, PMID: 20122406

Indiani C, Langston LD, Yurieva O, Goodman MF, O'Donnell M. 2009. Translesion DNA polymerases remodel the replisome and alter the speed of the replicative helicase. *PNAS* **106**:6031-6038. DOI: https://doi.org/10.1073/pnas.0901403106, PMID: 19279203

Kang YH, Farina A, Bermudez VP, Tappin I, Du F, Galal WC, Hurwitz J. 2013. Interaction between human Ctf4 and the Cdc45/Mcm2-7/GINS (CMG) replicative helicase. *PNAS* **110**:19760-19765. DOI: https://doi.org/10.1073/pnas.1320202110, PMID: 24255107

802 Kilkenny ML, Simon AC, Mainwaring J, Wirthensohn D, Holzer S, Pellegrini L. 2017. The human
803 CTF4-orthologue AND-1 interacts with DNA polymerase alpha/primase via its unique C-terminal HMG
804 box. *Open Biol* **7**.10. DOI: https://doi.org/10.1098/rsob.170217, PMID: 29167311
805
806 Kitamura E, Blow JJ, Tanaka TU. 2006. Live-cell imaging reveals replication of individual replicons in
807 eukaryotic replication factories. *Cell* **125**:1297-1308. DOI: https:// doi.org/10.1016/j.cell.2006.04.041,
808 PMID: 16814716
809
810 Kose HB, Larsen NB, Duxin JP, Yardimci H. 2019. Dynamics of the Eukaryotic Replicative Helicase at
811 Lagging-Strand Protein Barriers Support the Steric Exclusion Model. Cell Rep. **26**:2113-2125. doi:
812 10.1016/j.celrep.2019.01.086. PMID 30784593.

813 Kurat CF, Yeeles JTP, Patel H, Early A, Diffley JFX. 2017. Chromatin Controls DNA Replication
814 Origin Selection, Lagging-Strand Synthesis, and Replication Fork Rates. Mol Cell. **65**:117-130. doi:
815 10.1016/j.molcel.11.016. Epub 2016 Dec 15. PMID: 27989438.

816 Langston L, O'Donnell M. 2017a. Action of CMG with strand-specific DNA blocks supports an internal
817 unwinding mode for the eukaryotic replicative helicase. *Elife* **6**:e23449. DOI:
818 https://doi.org/10.7554/eLife.23449, PMID: 28346143
819
820 Langston LD, Mayle R, Schauer GD, Yurieva O, Zhang D, Yao NY, Georgescu RE, O'Donnell ME.
821 (2017b) Mcm10 promotes rapid isomerization of CMG-DNA for replisome bypass of lagging strand
822 DNA blocks. Elife. **6**: e29118. doi: 10.7554/eLife.29118. PMID: 28869037.
823
824 Langston LD, Zhang D, Yurieva O, Georgescu RE, Finkelstein J, Yao NY, Indiani C, O'Donnell ME.
825 2014. CMG helicase and DNA polymerase epsilon form a functional 15-subunit holoenzyme for
826 eukaryotic leading-strand DNA replication. *PNAS* **111**:15390-15395. DOI:
827 https://doi.org/10.1073/pnas.1418334111, PMID: 25313033
828
829 Lewis JS, Spenkelink LM, Jergic S, Wood EA, Monachino E, Horan NP, Duderstadt KE, Cox MM,
830 Robinson A, Dixon NE, van Oijen AM. 2017. Single-molecule visualization of fast polymerase
831 turnover in the bacterial replisome. Elife. **6**. pii: e23932. doi: 10.7554/eLife.23932. PMID: 28432790
832
833 Li H, O'Donnell ME. 2018. The Eukaryotic CMG Helicase at the Replication Fork: Emerging
834 Architecture Reveals an Unexpected Mechanism. *Bioessays* **40**. DOI:
835 https://doi.org/10.1002/bies.201700208, PMID: 29405332
836
837 Ligasova A, Raska I, Koberna K. 2009. Organization of human replicon: singles or zipping couples? *J*
838 *Struct Biol* **165**:204-213. DOI: https://doi.org/10.1016/j.jsb.2008.11.004, PMID: 19063972
839
840 Madamba E.V., Berthet E.B., Francis N.J. 2017. Inheritance of Histones H3 and H4 during DNA
841 Replication In Vitro. Cell Rep. **21**:1361-1374. doi: 10.1016/j.celrep.2017.10.033. PMID: 29091772.
842
843 Mangiameli SM, Cass JA, Merrikh H, Wiggins PA. 2018. The bacterial replisome has factory-like
844 localization. Curr Genet. **64**(5):1029-1036. DOI: 10.1007/s00294-018-0830-z. Epub 2018 Apr 9. PMID:
845 29632994.
846

Mangiameli SM, Veit BT, Merrikh H, Wiggins PA. 2017. The Replisomes Remain Spatially Proximal throughout the Cell Cycle in Bacteria. PLoS Genet. **13**(1):e1006582. DOI: 10.1371/journal.pgen.1006582. eCollection 2017 Jan. PMID: 2811437.

Miles J, Formosa T. 1992. Evidence that POB1, a Saccharomyces cerevisiae protein that binds to DNA polymerase alpha, acts in DNA metabolism in vivo. *Mol Cell Biol* **12**:5724-5735. DOI: https://doi.org/10.1128/MCB.12.12.5724, PMID: 1448101

Moyer SE, Lewis PW, Botchan MR. 2006. Isolation of the Cdc45/Mcm2-7/GINS (CMG) complex, a candidate for the eukaryotic DNA replication fork helicase. *PNAS* **103**:10236-10241. DOI: https://doi.org/10.1073/pnas.0602400103, PMID: 16798881.

Natsume T, Tanaka TU. 2010. Spatial regulation and organization of DNA replication within the nucleus. *Chromosome Res* **18**:7-17. DOI: https://doi.org/10.1007/s10577-009-9088-0, PMID: 19856119

Nunez-Ramirez R, Klinge S, Sauguet L, Melero R, Recuero-Checa MA, Kilkenny M, Perera RL, Garcia-Alvarez B, Hall RJ, Nogales E, Pellegrini L, Llorca O. 2011. Flexible tethering of primase and DNA Pol alpha in the eukaryotic primosome. *Nucleic Acids Res* **39**:8187-8199. DOI: https://doi.org/10.1093/nar/gkr534, PMID: 21715379

O'Donnell M, Langston L, Stillman B. 2013. Principles and concepts of DNA replication in bacteria, archaea, and eukarya. *Cold Spring Harb Perspect Biol* **5**::a010108. DOI: https://doi.org/10.1101/cshperspect.a010108, PMID: 23818497
O'Donnell ME, Li H. 2018. The ring-shaped hexameric helicases that function at DNA replication forks. *Nat Struct Mol Biol* **25**:122-130. DOI: https://doi.org/10.1038/s41594-018-0024-x, PMID: 29379175

Perera RL, Torella R, Klinge S, Kilkenny ML, Maman JD, Pellegrini L. 2013. Mechanism for priming DNA synthesis by yeast DNA Polymerase alpha. *Elife* **2**:e00482. DOI: https://doi.org/10.7554/eLife.00482, PMID: 23599895

Pettersen EF, Goddard TD, Huang CC, Couch GS, Greenblatt DM, Meng EC, Ferrin TE. 2004. UCSF Chimera--a visualization system for exploratory research and analysis. *J Comput Chem* **25**:1605-1612. DOI: https://doi.org/10.1002/jcc.20084, PMID: 15264254

Petryk, N., Dalby, M., Wenger, A., Stromme, C.B., Strandsby, A., Andersson, R., and Groth, A. (2018). MCM2 promotes symmetric inheritance of modified histones during DNA replication. Science **361**, 1389-1392. doi: 10.1126/science.aau0294. Epub 2018 Aug 16. PMID:30115746.

Pope BD, Hiratani I, Gilbert DM. 2010. Domain-wide regulation of DNA replication timing during mammalian development. *Chromosome Res* **18**:127-136. DOI: https://doi.org/10.1007/s10577-009-9100-8, PMID: 20013151

Richet, N., Liu, D., Legrand, P., Velours, C., Corpet, A., Gaubert, A., Bakail, M., Moal-Raisin, G., Guerois, R., Compper, C., et al. (2015). Structural insight into how the human helicase subunit MCM2 may act as a histone chaperone together with ASF1 at the replication fork. Nucleic Acids Res. **43**, 1905–1917. doi: 10.1093/nar/gkv021. Epub 2015 Jan 23, PMID:25618846, PMCID: PMC4330383.

Rohou A, Grigorieff N. 2015. CTFFIND4: Fast and accurate defocus estimation from electron micrographs. *J Struct Biol* **192**:216-221. DOI: https://doi.org/10.1016/j.jsb.2015.08.008, PMID: 26278980

Samora CP, Saksouk J, Goswami P, Wade BO, Singleton MR, Bates PA, Lengronne A, Costa A, Uhlmann F. 2016. Ctf4 Links DNA Replication with Sister Chromatid Cohesion Establishment by Recruiting the Chl1 Helicase to the Replisome. *Mol Cell* **63**:371-384. DOI: https://doi.org/10.1016/j.molcel.2016.05.036, PMID: 27397686

Saner N, Karschau J, Natsume T, Gierlinski M, Retkute R, Hawkins M, Nieduszynski CA, Blow JJ, de Moura AP, Tanaka TU. 2013. Stochastic association of neighboring replicons creates replication factories in budding yeast. *J Cell Biol* **202**:1001-1012. DOI: https://doi.org/10.1083/jcb.201306143, PMID: 24062338

Scheres SH. 2012. RELION: implementation of a Bayesian approach to cryo-EM structure determination. *J Struct Biol* **180**:519-530. DOI: https://doi.org/10.1016/j.jsb.2012.09.006, PMID: 23000701

Simon AC, Zhou JC, Perera RL, van Deursen F, Evrin C, Ivanova ME, Kilkenny ML, Renault L, Kjaer S, Matak-Vinkovic D, Labib K, Costa A, Pellegrini L. 2014. A Ctf4 trimer couples the CMG helicase to DNA polymerase alpha in the eukaryotic replisome. *Nature* **510**:293-297. DOI: https://doi.org/10.1038/nature13234, PMID: 24805245

Sun J, Shi Y, Georgescu RE, Yuan Z, Chait BT, Li H, O'Donnell ME. 2015. The architecture of a eukaryotic replisome. *Nat Struct Mol Biol* **22**:976-982. DOI: https://doi.org/10.1038/nsmb.3113, PMID: 26524492

Tanaka H, Katou Y, Yagura M, Saitoh K, Itoh T, Araki H, Bando M, Shirahige K. 2009a. Ctf4 coordinates the progression of helicase and DNA polymerase alpha. *Genes Cells* **14**:807-820. DOI: https://doi.org/10.1111/j.1365-2443.2009.01310.x, PMID: 19496828

Tanaka H, Kubota Y, Tsujimura T, Kumano M, Masai H, Takisawa H. 2009b. Replisome progression complex links DNA replication to sister chromatid cohesion in Xenopus egg extracts. *Genes Cells* **14**:949-963. DOI: https://doi.org/10.1111/j.1365-2443.2009.01322.x, PMID: 19622120

Villa F, Simon AC, Ortiz Bazan MA, Kilkenny ML, Wirthensohn D, Wightman M, Matak-Vinkovic D, Pellegrini L, Labib K. 2016. Ctf4 Is a Hub in the Eukaryotic Replisome that Links Multiple CIP-Box Proteins to the CMG Helicase. *Mol Cell* **63**:385-396. DOI: https://doi.org/10.1016/j.molcel.2016.06.009, PMID: 27397685

Williams DR, McIntosh JR. 2002. mcl1+, the Schizosaccharomyces pombe homologue of CTF4, is important for chromosome replication, cohesion, and segregation. *Eukaryot Cell* **1**:758-773. DOI: https://doi.org/10.1128/EC.1.5.758-773.2002, PMID: 12455694

Xu M, Long C, Chen X, Huang C, Chen S, Zhu B. (2010) Partitioning of histone H3–H4 tetramers during DNA replication-dependent chromatin assembly. Science. **328**:94–98. DOI: 10.1126/science.1178994 PubMed: 20360108

Yardimci H, Loveland AB, Habuchi S, van Oijen AM, Walter JC. 2010. Uncoupling of sister replisomes during eukaryotic DNA replication. *Mol Cell* **40**:834-840. DOI: https://doi.org/10.1016/j.molcel.2010.11.027, PMID: 21145490

Yeeles JT, Deegan TD, Janska A, Early A, Diffley JF. (2015) Regulated eukaryotic DNA replication origin firing with purified proteins. Nature. **519**:431-5. doi: 10.1038/nature14285. Epub 2015 Mar 4, PMID 25739503.

Yeeles JT, Janska A, Early A, Diffley JF. 2017. How the Eukaryotic Replisome Achieves Rapid and Efficient DNA Replication. *Mol Cell* **65**:105-116. DOI: https://doi.org/10.1016/j.molcel.2016.11.017, PMID: 27989442

Yoshizawa-Sugata N, Masai H. 2009. Roles of human AND-1 in chromosome transactions in S phase. *J Biol Chem* **284**:20718-20728. DOI: https://doi.org/10.1074/jbc.M806711200, PMID: 19439411

You Z, De Falco M, Kamada K, Pisani FM, Masai H. 2013. The mini-chromosome maintenance (Mcm) complexes interact with DNA polymerase alpha-primase and stimulate its ability to synthesize RNA primers. *PLoS One* **8**:e72408. DOI: https://doi.org/10.1371/journal.pone.0072408, PMID: 23977294.

Yuan Z, Bai L, Sun J, Georgescu R, Liu J, O'Donnell ME, Li H. 2016. Structure of the eukaryotic replicative CMG helicase suggests a pumpjack motion for translocation. *Nat Struct Mol Biol* **23**:217-224. DOI: https://doi.org/10.1038/nsmb.3170, PMID: 26854665

Zhang K. 2016. Gctf: Real-time CTF determination and correction. *J Struct Biol* **193**:1-12. DOI: https://doi.org/10.1016/j.jsb.2015.11.003, PMID: 26592709

Zheng SQ, Palovcak E, Armache JP, Verba KA, Cheng Y, Agard DA. 2017. MotionCor2: anisotropic correction of beam-induced motion for improved cryo-electron microscopy. *Nat Methods* **14**:331-332. DOI: https://doi.org/10.1038/nmeth.4193, PMID: 28250466

Zhou Y, Wang TS. 2004. A coordinated temporal interplay of nucleosome reorganization factor, sister chromatin cohesion factor, and DNA polymerase alpha facilitates DNA replication. *Mol Cell Biol* **24**:9568-9579. DOI: https://doi.org/10.1128/MCB.24.21.9568-9579.2004, PMID: 15485923

Zink D. 2006. The temporal program of DNA replication: new insights into old questions. *Chromosoma* **115**:273-287. DOI: https://doi.org/10.1007/s00412-006-0062-8, PMID: 16552593

Tables

Table1. Cryo-EM 3D reconstruction and refinement of the three $Ctf4_3$–CMG complexes.

	$Ctf4_3$–CMG_1 (EMD-20471) (PDB 6PTJ)	**$Ctf4_3$–CMG_2** (EMD-20472) (PDB 6PTN)	**$Ctf4_3$–CMG_3** (EMD-20473) (PDB 6PTO)
Data collection and processing			
Magnification	130,000	130,000	130,000
Voltage (kV)	300	300	300
Electron dose ($e^-/Å^2$)	50	50	50
Under-focus range (μm)	1.5 – 2.5	1.5 – 2.5	1.5 – 2.5
Pixel size (Å)	1.074	1.074	1.074
Symmetry imposed	C1	C1	C1
Initial particle images (no.)	759,267	759,267	759,267
Final particle images (no.)	200,491	53,853	53,117
Map resolution (Å)	3.8	5.8	7.0
FSC threshold	0.143	0.143	0.143
Map resolution range (Å)	3.5 – 5.0	5.0 – 8.0	5.0 – 8.0
Refinement			
Initial model used (PDB code)	3jc5, 4c8h	3jc5, 4c8h	3jc5, 4c8h
Map sharpening B factor ($Å^2$)	−146	−135	−143
Model composition			
Non-hydrogen atoms	34,366	90,831	131,141
Protein and DNA residues	41,92	11,221	15,710
Ligands	0	0	0
R.m.s. deviations			
Bond lengths (Å)	0.009		
Bond angels (°)	1.46		
Validation			
MolProbity score	2.05		
Clashscore	10.96		
Poor rotamers (%)	0.63		
Ramachandran plot			
Favored (%)	91.65		
Allowed (%)	8.16		
Disallowed (%)	0.19		

Table 2. Cryo-EM 3D reconstruction of the Ctf4$_3$–Pol α-primase complex.

	Ctf4$_3$–Polα-primase (EMD-XXXX)
Data collection and processing	
Magnification	120,000
Voltage (kV)	200
Electron dose (e^-/Å^2)	60
Under-focus range (μm)	1.5 – 2.5
Pixel size (Å)	1.21
Symmetry imposed	C1
Initial particle images (no.)	237,688
Final particle images (no.)	48,414
Map resolution (Å)	12
FSC threshold	0.143
Map resolution range (Å)	10 – 15

Video 1. A 360° rotation around a vertical axis of the 3D density map of 1CMG-Ctf4$_3$ at 3.8 Å resolution, followed by the subunit-segmented map, and the cartoon view of the atomic model. The map and model do not include the C-tier AAA+ motor ring of the Mcm2-7, which was excluded during 3D refinement.

Video 2. A 360° rotation of the 3D density map of 2CMG-Ctf4$_3$, at 5.8 Å resolution, followed by density segmentation, and then the atomic model of 2CMG-Ctf4$_3$.

Video 3. Combination of the structures of 2CMG-Ctf4$_3$ with Ctf4$_3$–Pol α-primase to generate a pseudo-atomic model of the 2CMG-Ctf4$_3$–1Pol α-primase core replicon factory, by overlapping the shared Ctf4$_3$ density of the 2CMG-Ctf4$_3$ and Ctf4$_3$–Pol α-primase structures. The final model is rotated 360° around a vertical axis.

Main Text Figures and Legends.

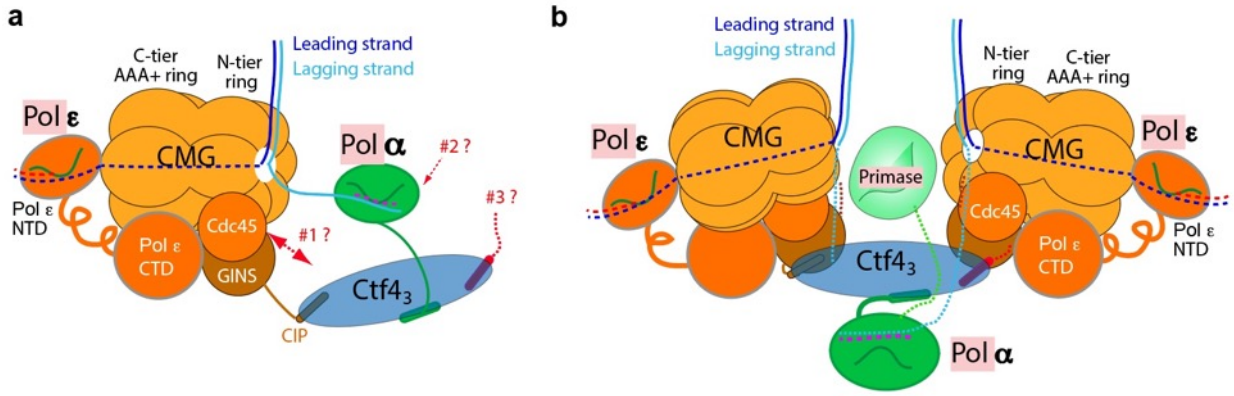

Figure 1. Comparison of individual replisomes and a replisome factory. (**a**) Individual replisome: $Ctf4_3$ connects CMG to Pol α-primase, and Pol ε binds the C-face of CMG. Three unanswered questions are represented by the three question marks: 1 – What components in CMG, in addition to the CIP peptide of Sld5, interact with $Ctf4_3$ to maintain their stable association? 2 – How does Pol α-primase interact with $Ctf4_3$ – on the top N-face or the bottom C-face of the Ctf4 disk? 3 – Can a second Pol α-primase also occupy the third CIP-site of $Ctf4_3$? (**b**). Factory model of two replisomes inferred from cryoEM structures of the current report. Two CMGs bind tightly to two subunits of the Ctf4 trimer by an extensive interface formed with the Psf2 and Cdc45 subunits of CMG. One Pol α-primase occupies the third Ctf4 subunit. The single Pol α -primase connects to the C-face of Ctf4 near the split points of DNA entering the N-faces of the two CMGs. The two leading Pol ε complexes bind the C-face of CMG on the outside perimeter of the factory. See text for details.

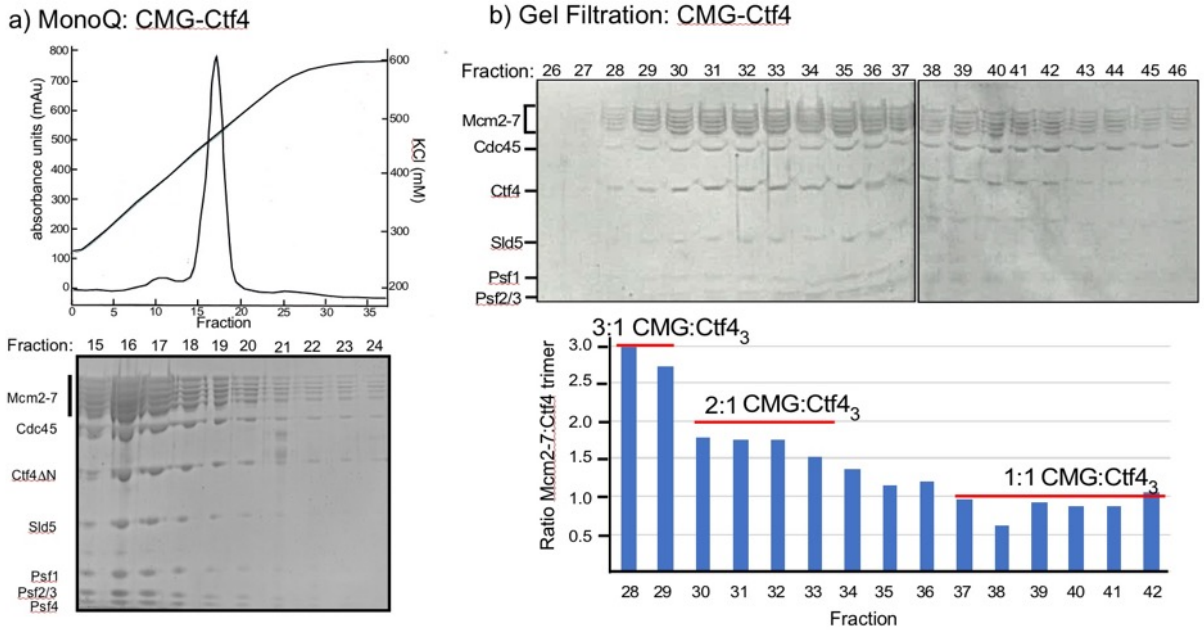

Figure 2. Multiple CMGs form a stable complex with the Ctf4 trimer. **(a)** A mixture of CMG and Ctf4$_3$ were applied to ion-exchange chromatography on a MonoQ column. The top panel shows the elution profile the CMG-Ctf4$_3$ complex(s) which elute at approximately 450 mM NaCl. **(b)** The SDS PAGE of gel filtration fractions from the MonoQ elution shows the CMG-Ctf4 complex(s) are stable during these chromatography steps and density scans indicate ratios of CMG:Ctf4$_3$ as indicated in the histogram. Glycerol gradient centrifugations also reveal a complex of CMG to Ctf4$_3$, as well as other complexes (**Figure 2 – figure supplement 1**).

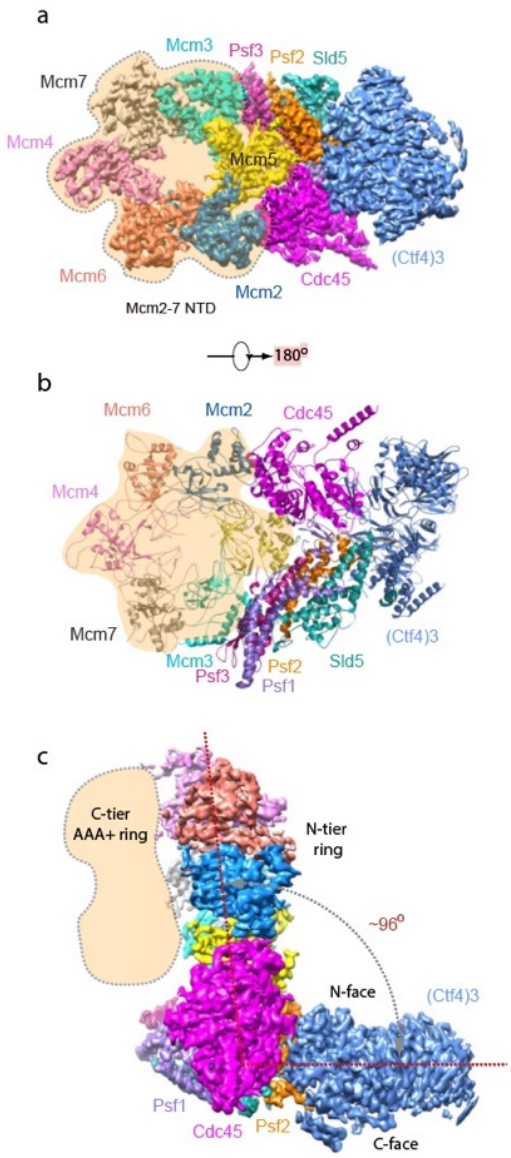

Figure 3. Cryo-EM structure of 1CMG-Ctf4$_3$. Cryo-EM density map of the 1CMG-Ctf4$_3$ complex in: **(a)** top view looking down the N-tier view of Mcm2-7. **(b)** Cartoon representation of the atomic model of 1CMG-Ctf4$_3$ in the C-tier AAA+ ring view. **(c)** Side view. Each subunit is colored differently. The Mcm2-7 AAA+ motor ring is flexible, and thus removed for higher resolution, but its position is shaded in beige. The resolution of this complex was facilitated by focused 3D refinement omitting the AAA+ C-tier of the Mcms in CMG (**Figure 3 – figure supplements 1 and 2**).

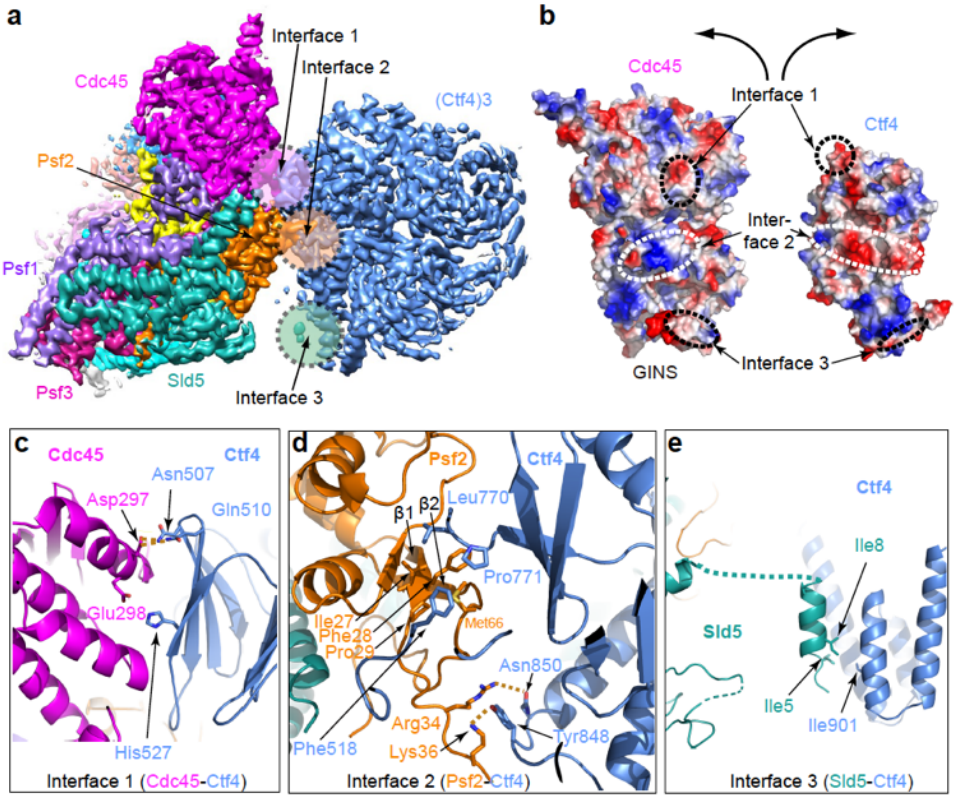

Figure 4. Molecular interface between Ctf4$_3$ and CMG. (**a**) 3D map showing the interacting Cdc45-GINS and Ctf4$_3$. Different subunits are in different colors as labeled, and the three interacting regions are labeled Interfaces 1 through 3. (**b**) An open-book view of the interface between Cdc45–GINS and Ctf4$_3$, shown in the electrostatic surface view. The three contacting regions between Cdc45–GINS and Ctf4 are marked by three pairs of dashed ellipses. (**c-e**) Interface 1 between Cdc45 and Ctf4 (**c**), interface 2 between Psf2 and Ctf4 (**d**) , and interface 3 between Sld5 and Ctf4 (**e**), shown in cartoon view with several interacting residues shown in sticks. A close-up view of the interfaces is shown in **Figure 4 – figure supplements 1 and 2**. Conservation in the interface region is shown in **Figure 4 – figure supplement 3**.

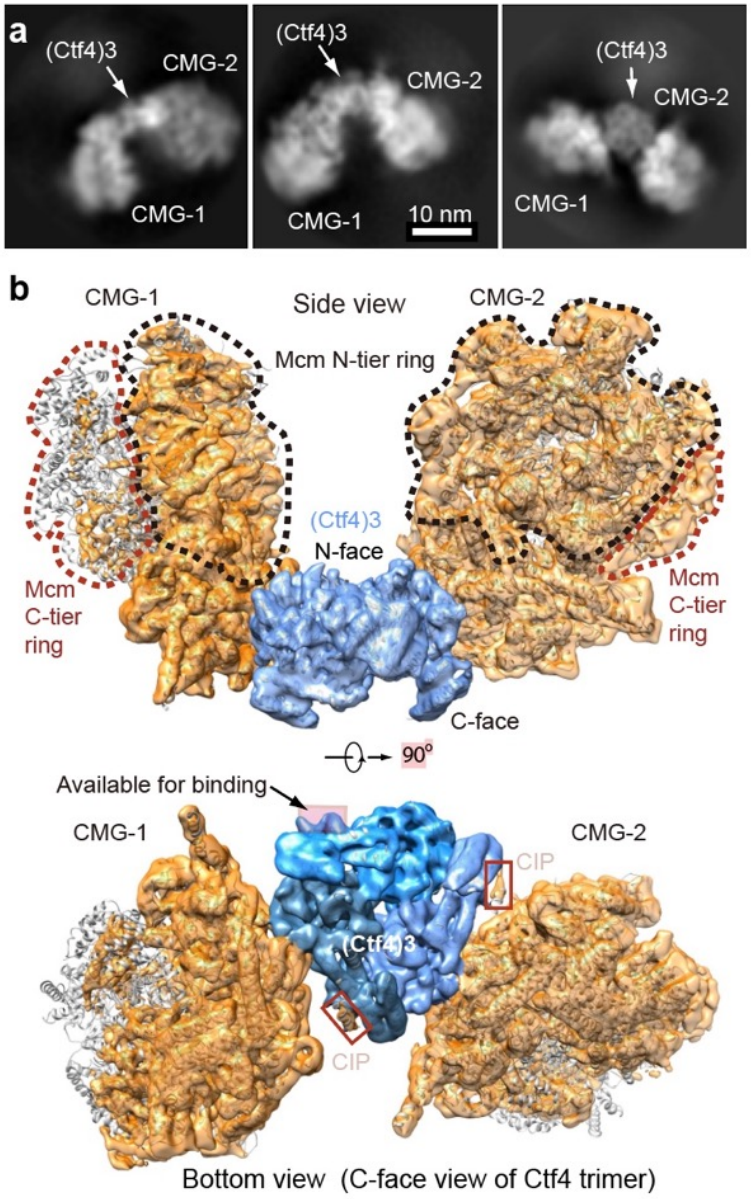

Figure 5. Cryo-EM structure of 2CMG-Ctf4$_3$. (**a**) Selected 2D class averages of cryo-EM images of 2CMG-Ctf4$_3$. (**b**) A side and a bottom view of the 3D map with docked atomic models of Ctf4$_3$ and CMG shown in cartoon view. The C-tier AAA+ ring of Mcm2-7 is partially flexible and the density is invisible at the surface rendering threshold used. See also **Figure 5 – figure supplements 1 and 2** and **Video 2**.

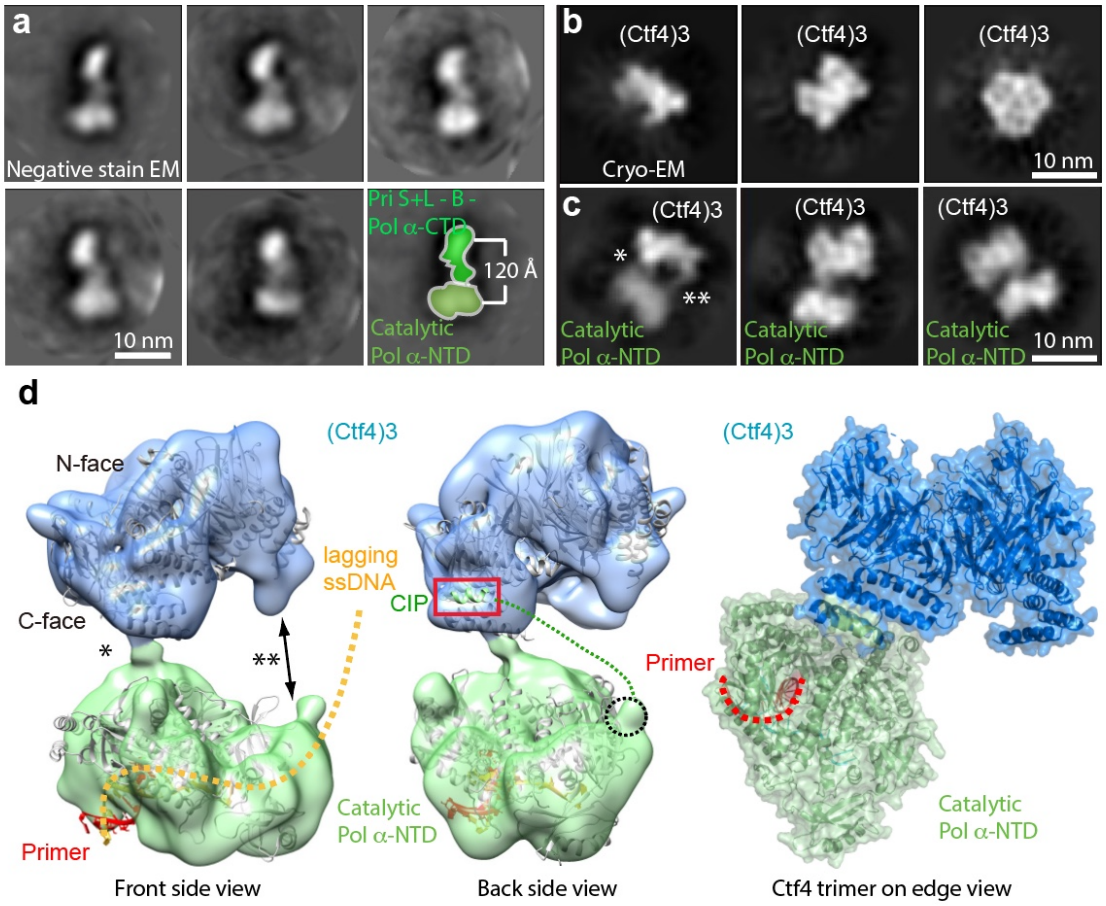

Figure 6. Cryo-EM map of $Ctf4_3$–Pol α-primase. (**a**) Selected 2D class averages of negatively stained images of Pol α-primase showing the enzyme in a similar view with a two-lobed architecture. (**b**) 2D class averages of cryo-EM images of $Ctf4_3$ in three distinct views. (**c**) Three selected 2D class averages of cryo-EM images of $Ctf4_3$–Pol α-primase. Note the primase lobe of $Ctf4_3$–Pol α-primase is not visible. (**d**) Left and middle panels: front and back views of the surface-rendered cryo-EM 3D map of $Ctf4_3$–Pol α-primase docked with the crystal structure of Ctf4 in light blue and crystal structure of the catalytic Pol α-NTD in light green. Right panel: atomic model viewed when the Ctf4 trimer is orientated horizontal and on edge. Rigid body docking is further presented in **Figure 6 – figure supplement 1**. The asterisk (*) and double asterisk (**) in (**c, d**) mark the left and right contacts, respectively, between $Ctf4_3$ and Pol α-NTD. The right contact is not visible in the 3D map (**d**). Increasing the concentration of Pol α-primase did not give additional Pol α-primase bound to Ctf4 (**Figure 6 – figure supplement 2**).

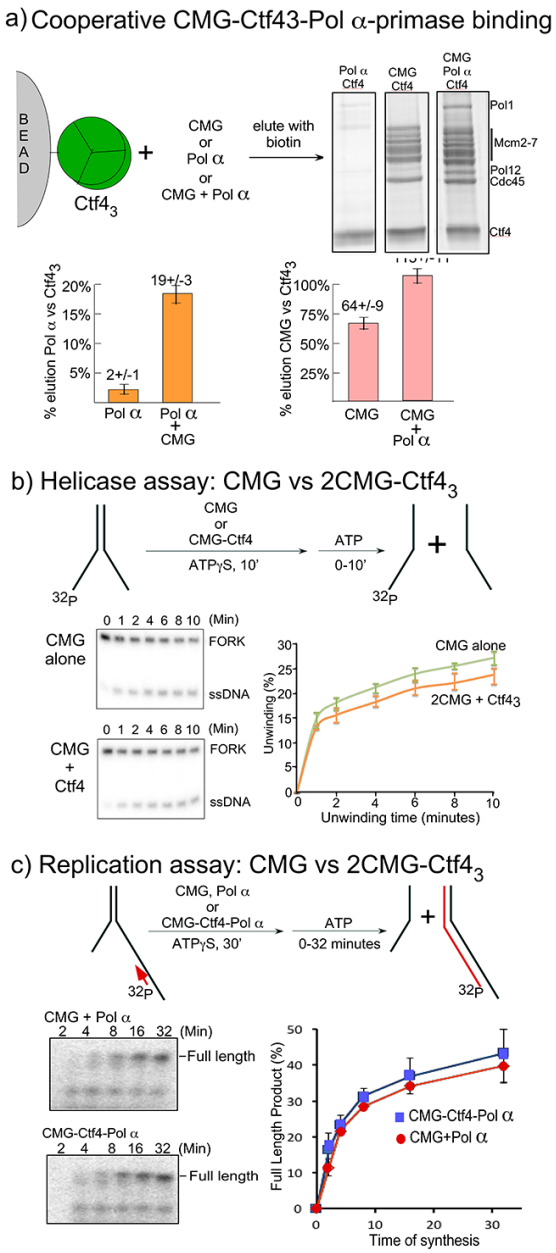

Figure 7. Cooperative assembly of the CMG-Ctf4$_3$-Pol α-primase complex. (a) Streptag-Ctf4 trimer on streptactin magnetic beads was added to either Pol α, CMG or a mix of Pol α + CMG. Proteins were eluted with biotin and analyzed by SDS PAGE (upper right). The assay was repeated in triplicate and gel scans were quantitated (below). Error bars show the standard deviation. **(b-c).** Both CMGs in the 2CMG-Ctf4$_3$ factory are active. **(b)** Top: Scheme of the helicase assay. CMG or a 2CMG+1Ctf4$_3$ mix were preincubated with forked DNA and 0.1 mM ATPγS for 10 min, followed by 5 mM ATP. Ten minutes is sufficient for CMG to bind the DNA as shown in **Figure 7 – figure supplement 3**. Bottom: Representative time courses of helicase activity are shown in the native PAGE gels (left), and results of triplicate assays are shown in the plot (right). Results of additional CMG:Ctf4 ratios are shown in **Figure 7 – figure supplement 3a**. **(c)** Scheme of the replication assay. CMG or a 2CMG+1Ctf4$_3$ mix were preincubated with Pol α-primase, ^{32}P-primed fork DNA and 0.1 mM ATPγS for 30', followed by 5 mM ATP, 4 mM dNTPs. 30 min is sufficient for CMG and Pol α-primase to bind the primed forked DNA as shown in **Figure 7 - figure supplement 4a**. Bottom: Representative time courses of replication activity are shown in the gels (left) and results of triplicate assays are shown in the plot (right). Additional replication assays of preformed CMG-Ctf4$_3$ complexes are shown in **Figure 7 – figure supplement 4b**.

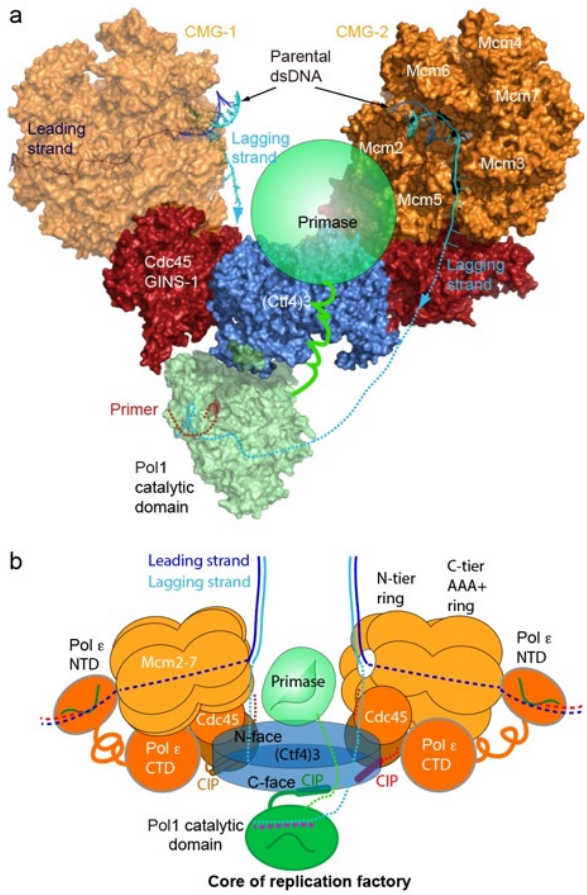

Figure 8. A model for the coupled sister replisomes. (**a**) A composite atomic model of one Pol α-primase and two CMG helicases organized in a core factory with a Ctf4 trimer. The model is derived by aligning $Ctf4_3$ shared between the $Ctf4_3$-CMG dimer model and the model of $Ctf4_3$-Pol α NTD. The DNA structure is based on the structure of CMG-forked DNA (PDB 5U8S), but the lagging strand outside the CMG channel is modeled. The possible location of the primase module of Pol α-primase is indicated by a green ellipse. (**b**) A sketch illustrating the leading strand Pol ε at the C-tier face of the CMG helicase and the primase reaches atop the N-face of $Ctf4_3$, potentially capable of priming both the lagging strands. See text for details. See also **Figure 8 – figure supplements 1, 2**, and **Video 3**.

Figure Supplements and their legends:

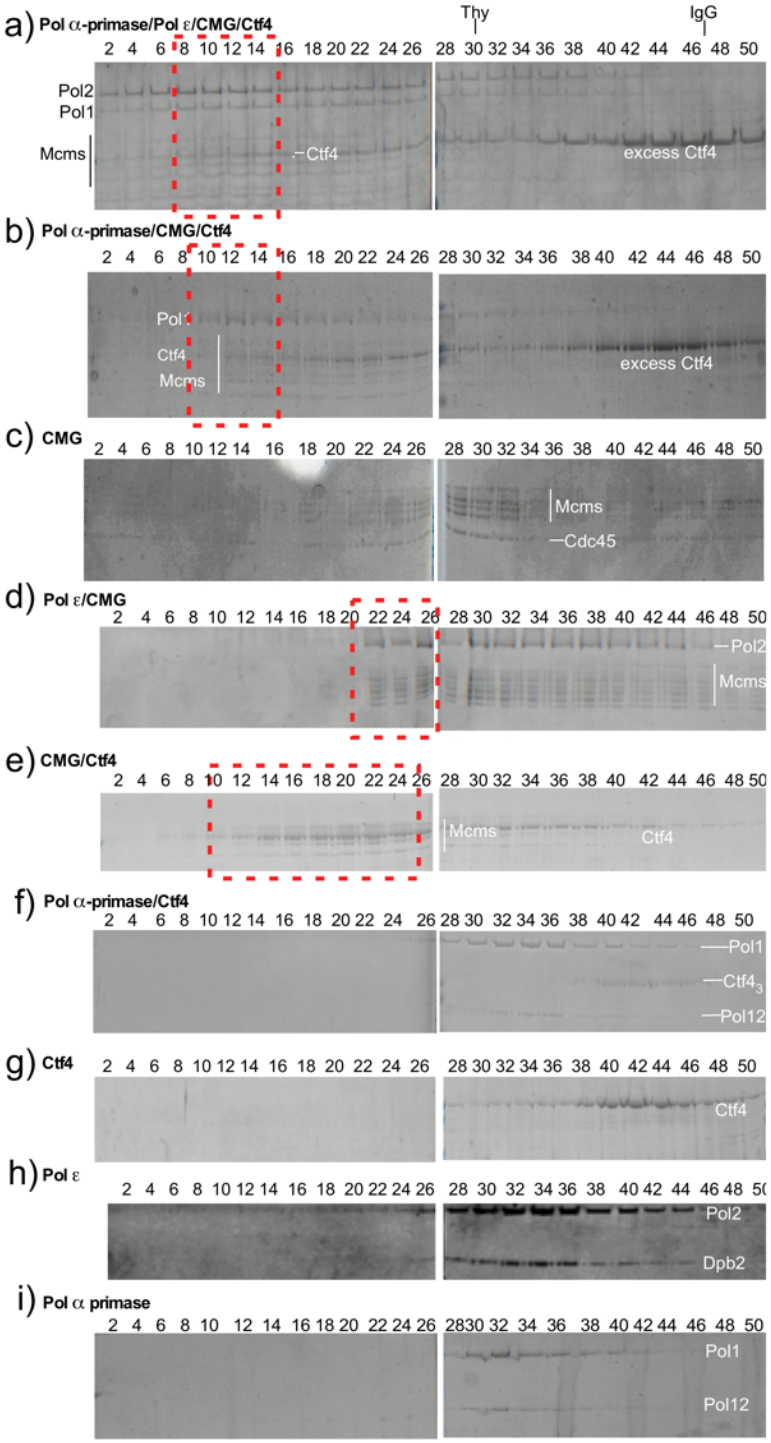

Figure 2 - figure supplement 1. Reconstitution of replisome complexes. Glycerol gradient sedimentation of different protein mixtures. Panels a and b (red boxes), compared to panels c-i, indicate that Ctf4 promotes large super-complexes containing CMG and DNA polymerases. Pol ε binds CMG in the absence of $Ctf4_3$ (red box, panel d), and $Ctf4_3$ binds CMG (red box, panel e) as noted by the significant shift to a higher mw complex. Migration of protein standards, Thyroglobulin (Thy) and IgG, are shown at the top.

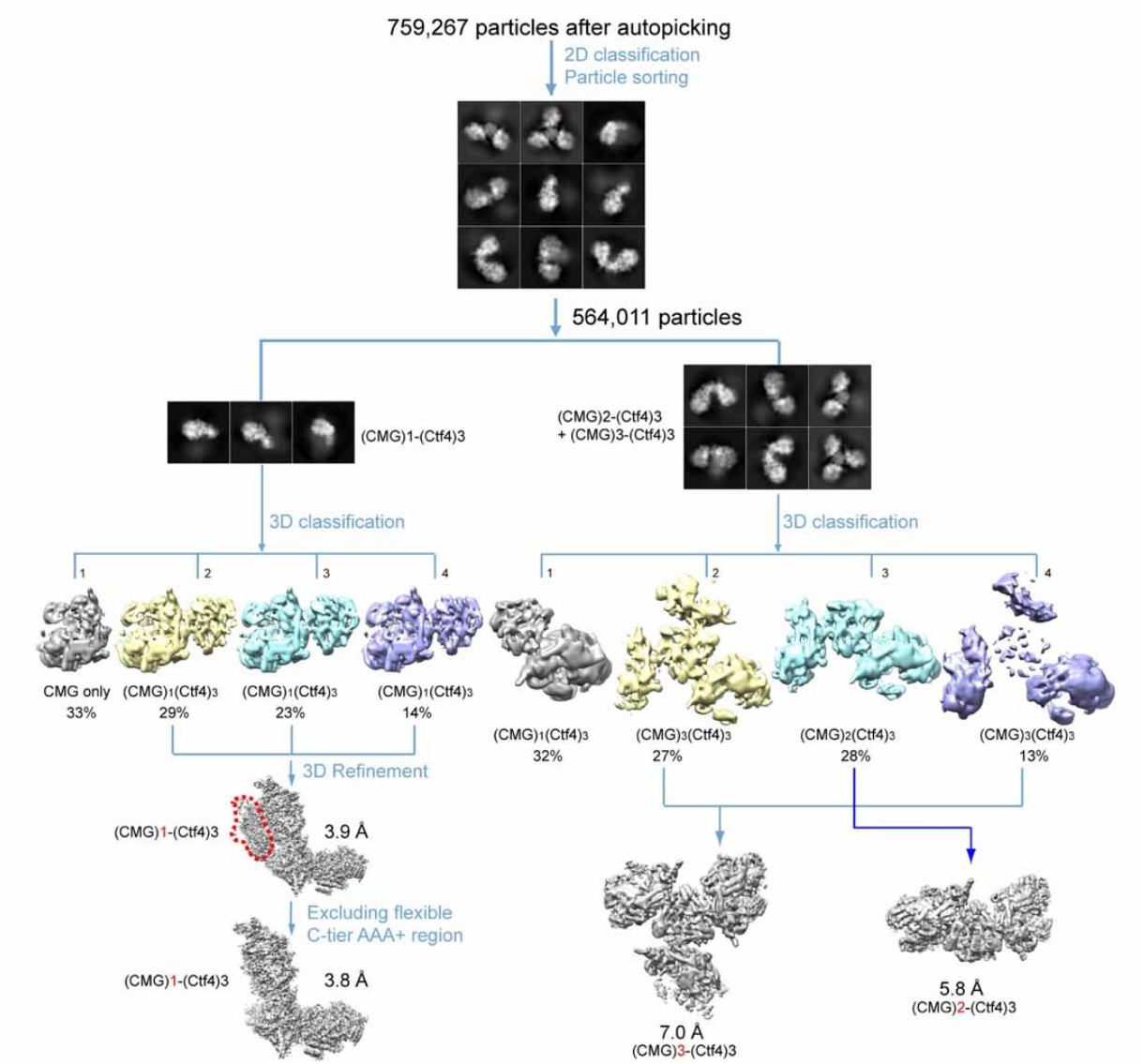

Figure 3 – figure supplement 1. Image processing and 3D reconstruction scheme. Extensive 2D and 3D classifications led to reconstruction of 3D maps of the 1CMG-Ctf4$_3$ complex$_1$ at 3.8 Å resolution, the 2CMG-Ctf4$_3$ complex at 5.8 Å resolution, and the3CMG- Ctf4$_3$ complex at 7.0 Å resolution.

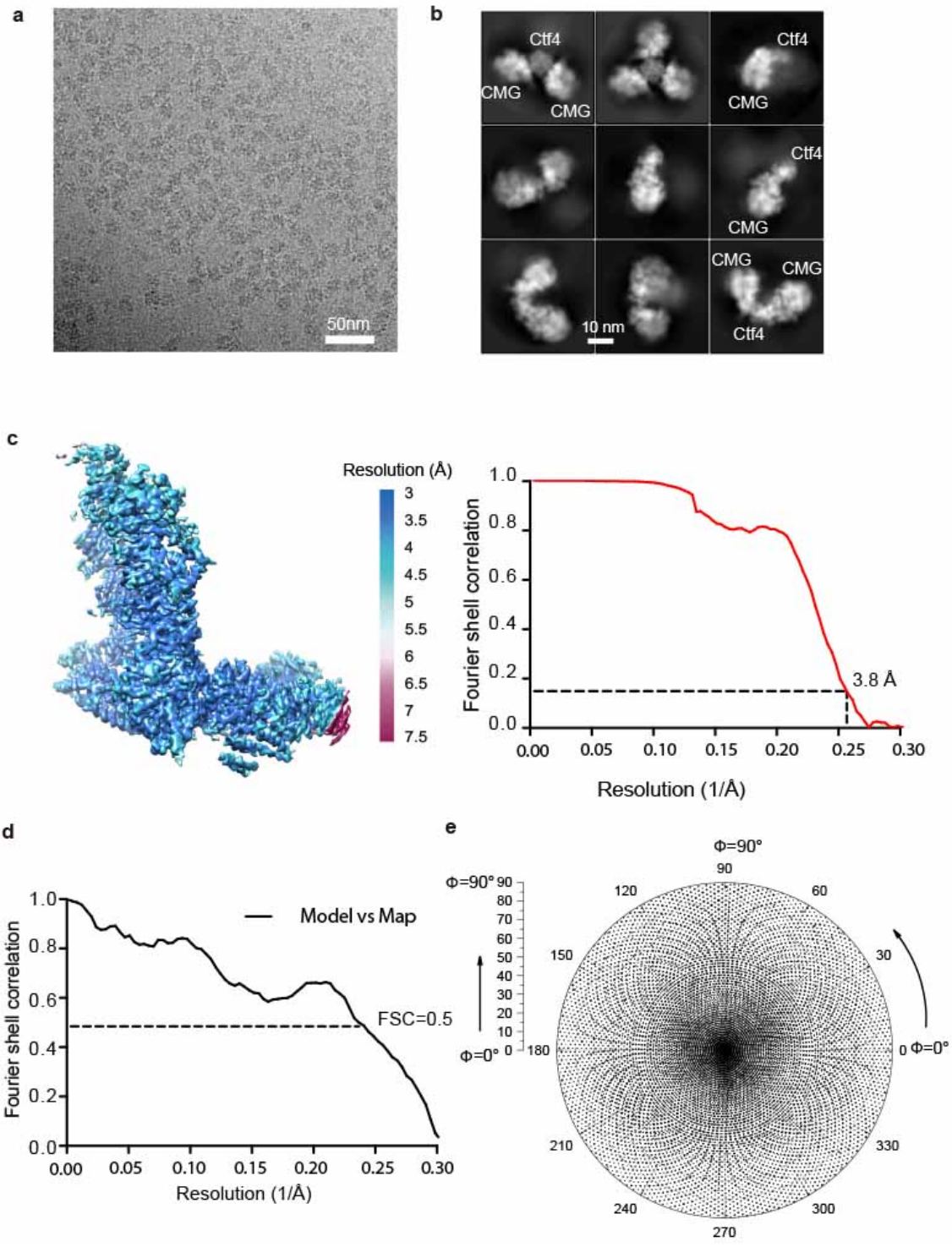

Figure 3 – figure supplement 2. Image processing and resolution estimation of the 3D map of the 1CMG-Ctf4$_3$ complex. (**a**) A typical raw micrograph. (**b**) 2D classification reveals the presence of 1, 2 or 3 copies of CMG helicase in complex with Ctf4$_3$. (**c**) Color-coded surface rendering of the 3D map (left panel) and the gold-standard Fourier shell correlation curve (right panel) of the 1CMG-Ctf4$_3$ complex masking out the flexible C-tier motor ring of the Mcm2-7. (**d**) Gold-standard Fourier shell correlation of the atomic model versus the 3d map. (**e**) Euler angle distribution of the raw particles used in 3D reconstruction.

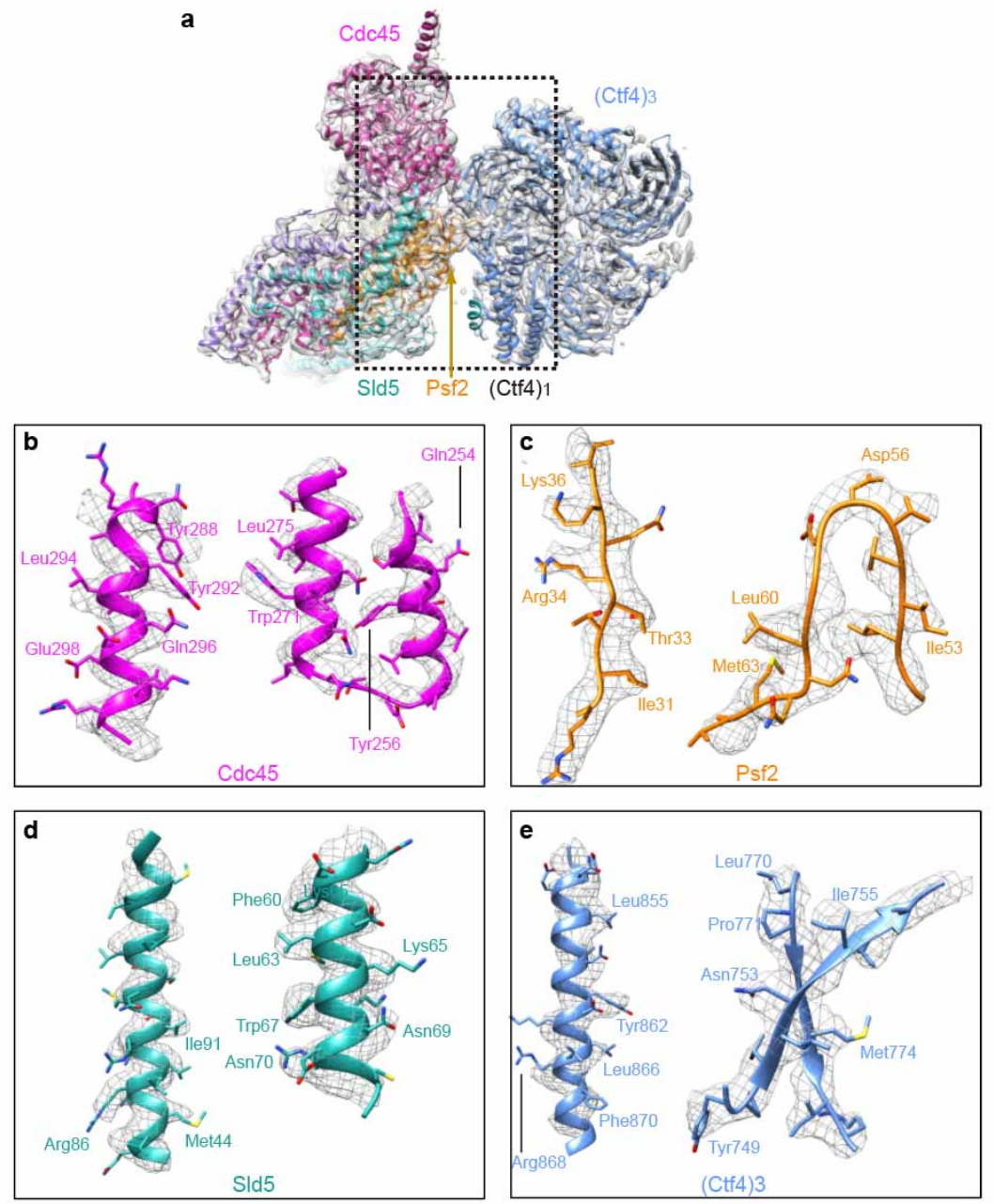

Figure 4 – figure supplement 1. Detailed densities at selected regions in the 3D map of $Ctf4_3$–CMG_1 complex. (**a**) 3D density showing the $Ctf4_3$–Cdc45–GINS, by omitting the Mcm2-7 density in the 3d map, superimposed with the atomic model. Each subunit is colored differently and as labeled. (**b-e**) Two example regions in Cdc45 (**b**), Psf2 (**c**), Sld5 (**d**), and Ctf4 (**e**) with several side chains shown as sticks.

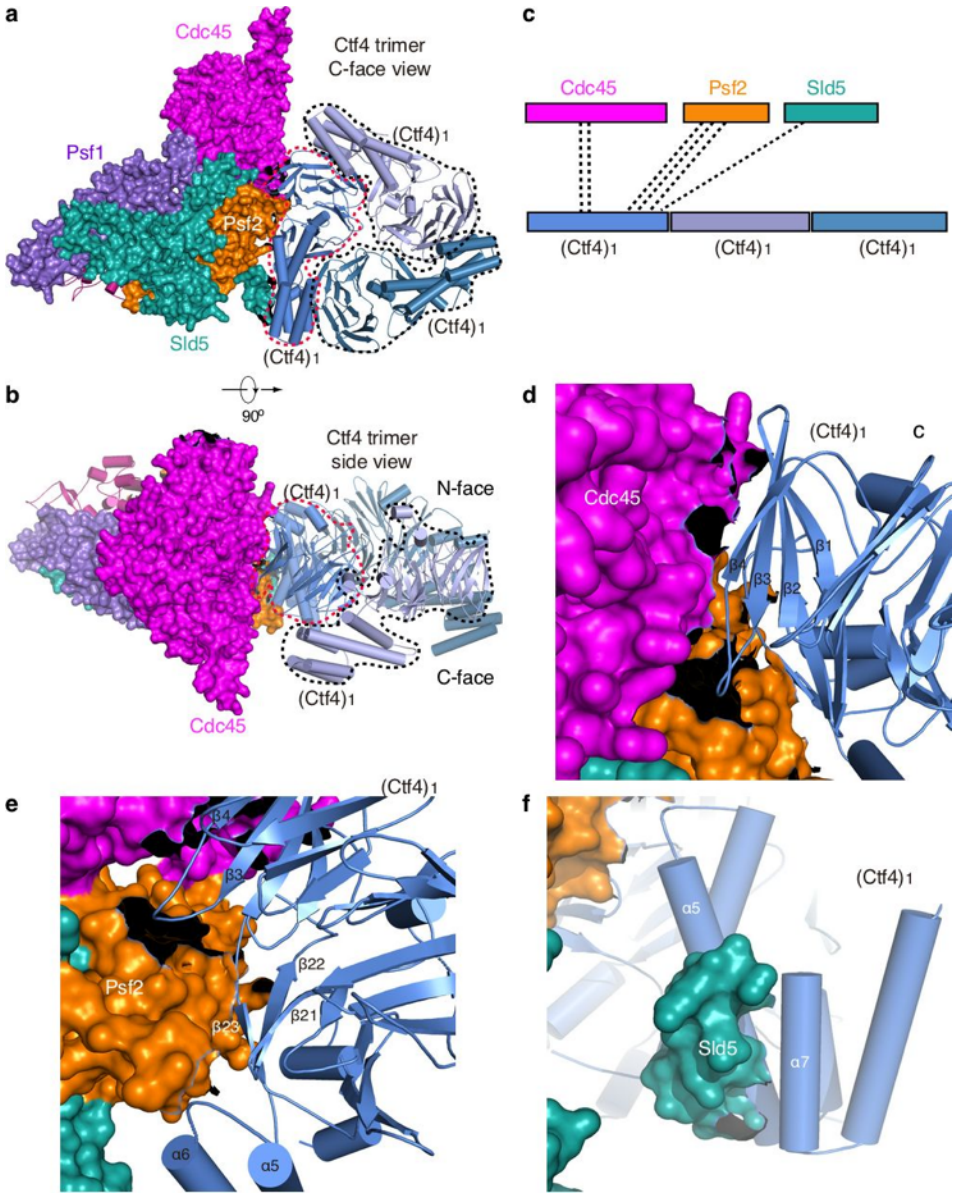

Figure 4 – figure supplement 2. Only one Ctf4 subunit engages with Cdc45 and GINS of one CMG helicase. The 1CMG-Ctf4$_3$ structure viewed from the C-face (**a**) and side (**b**) of the Ctf4$_3$ disk. Cdc45 and GINS are shown in surface and the Ctf4$_3$ in cartoon. The interacting Ctf4 monomer is demarcated by a dashed red curve, and the remaining two non-interacting monomers by dashed black curves. (**c**) A sketch showing Cdc45 and GINS interact with only one Ctf4 monomer. (**d-f**) Interfaces between the interacting Ctf4 monomer and Cdc45 (**d**), Psf2 (**e**), and Sld5 (**f**).

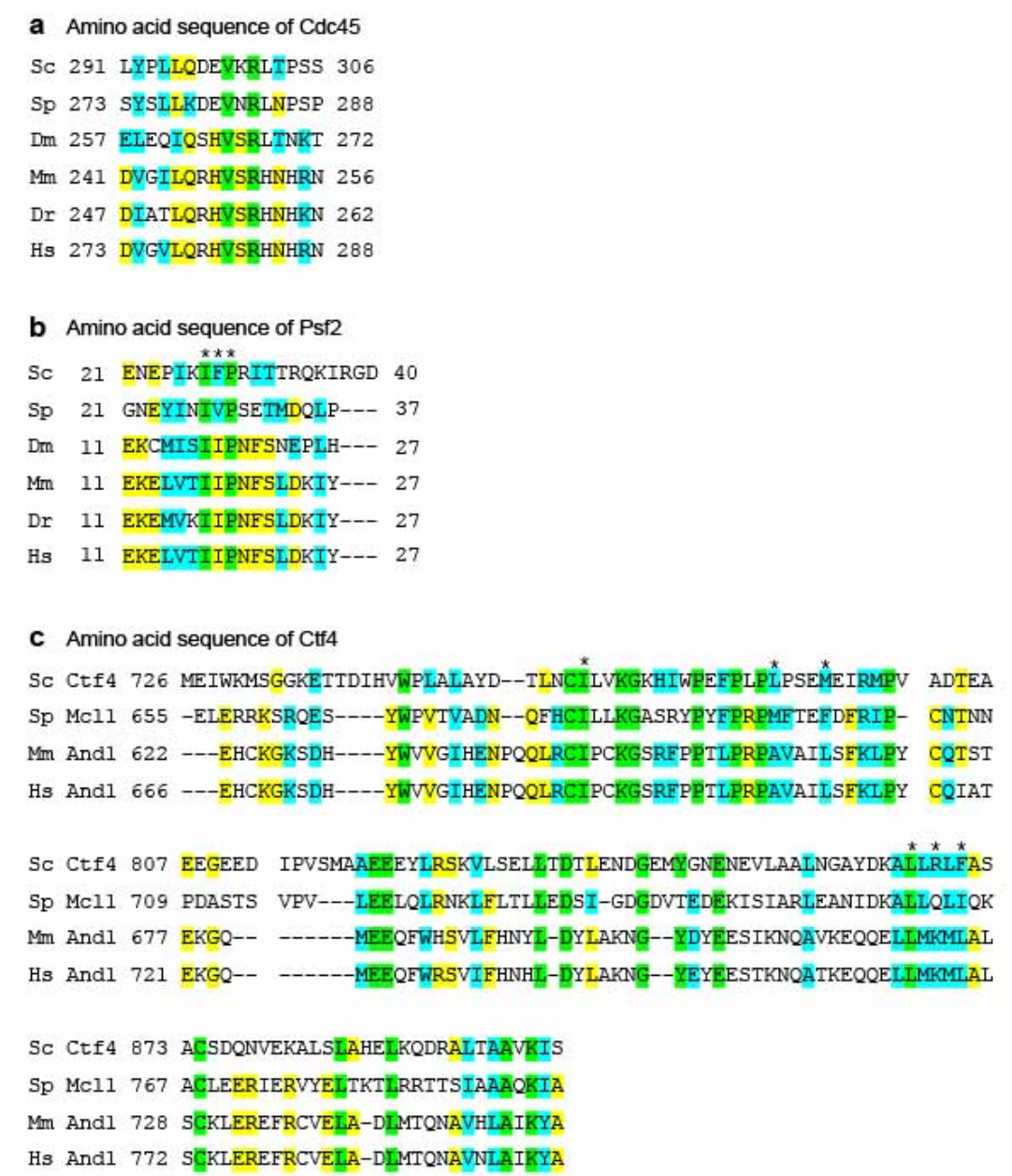

Figure 4 – figure supplement 3. Sequence alignment of the Ctf4-contacting regions in CMG, Psf2 and Cdc45. (a) Conserved sequences in Cdc45 that contact Ctf4. **(b)** Conserved sequences in Psf2 that contact Ctf4. **(c)** Conserved sequences in Cdc45 that contact Psf2 and Cdc45. The asterisks mark the conserved hydrophobic residue at the interface between Psf2 and Ctf4. Sc: *Saccharomyces cerevisiae*; Sp: *Saccharomyces pombe*; Dm: *Drosophila melanogaster*; Mm: *Mus musculus*; Dr: *Danio rerio*, Hs: *Homo sapiens*. Invariant residues are highlighted in green, identical residues in Yellow, and similar residues in cyan.

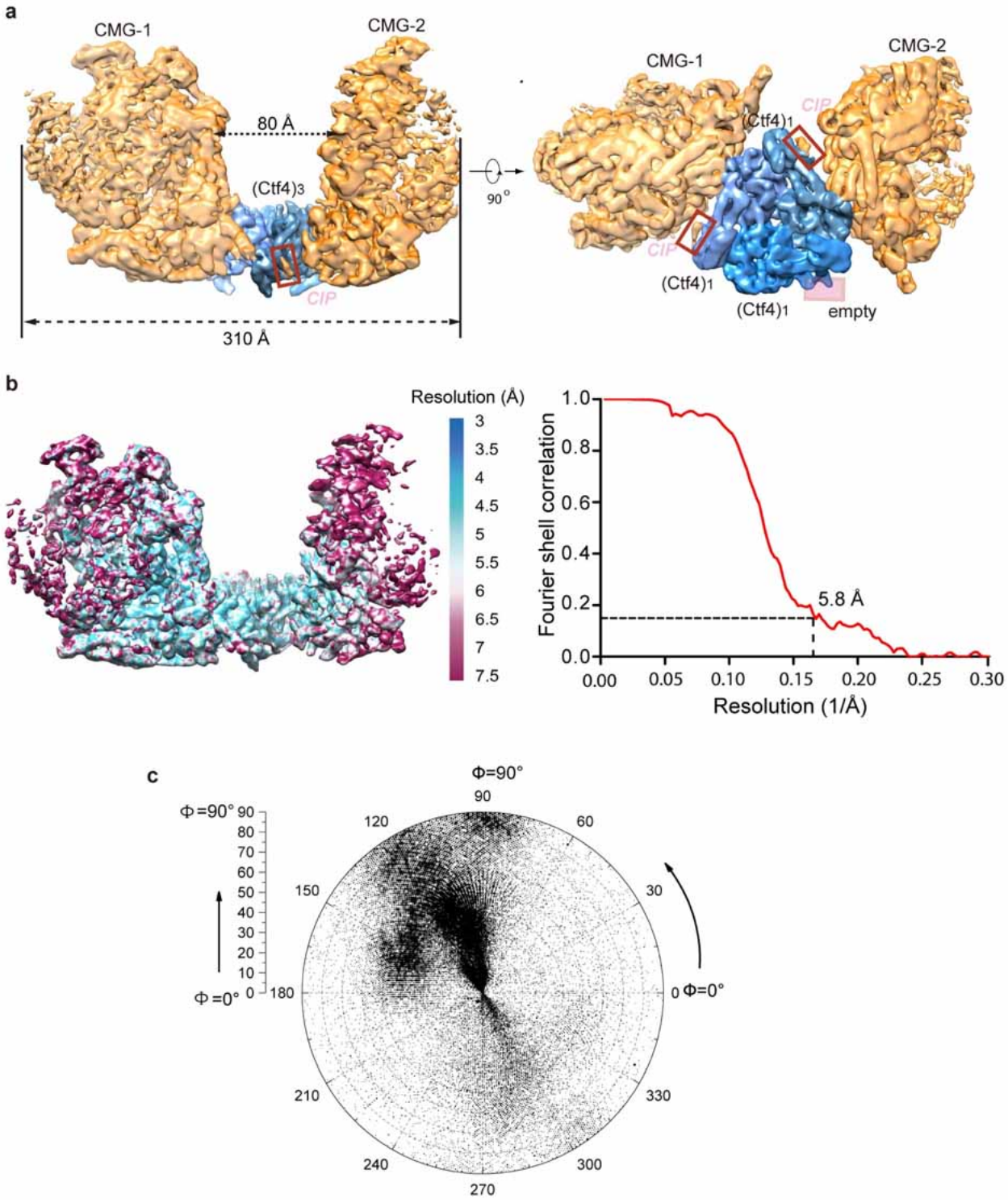

Figure 5 – figure supplement 1. 3D map and resolution estimation of Ctf4$_3$ in complex with two CMG. (**a**) Surface-rendered 3D map of 2CMG-Ctf4$_3$ in side view (left) and bottom view from the C-face of Ctf4$_3$ (right), (**b**) Color-coded 3D map of 2CMG-Ctf4$_3$ according to the local resolution (left) and the gold-standard Fourier shell correlation of the two half maps. (**c**) Euler angle distribution of raw particles used in 3D reconstruction.

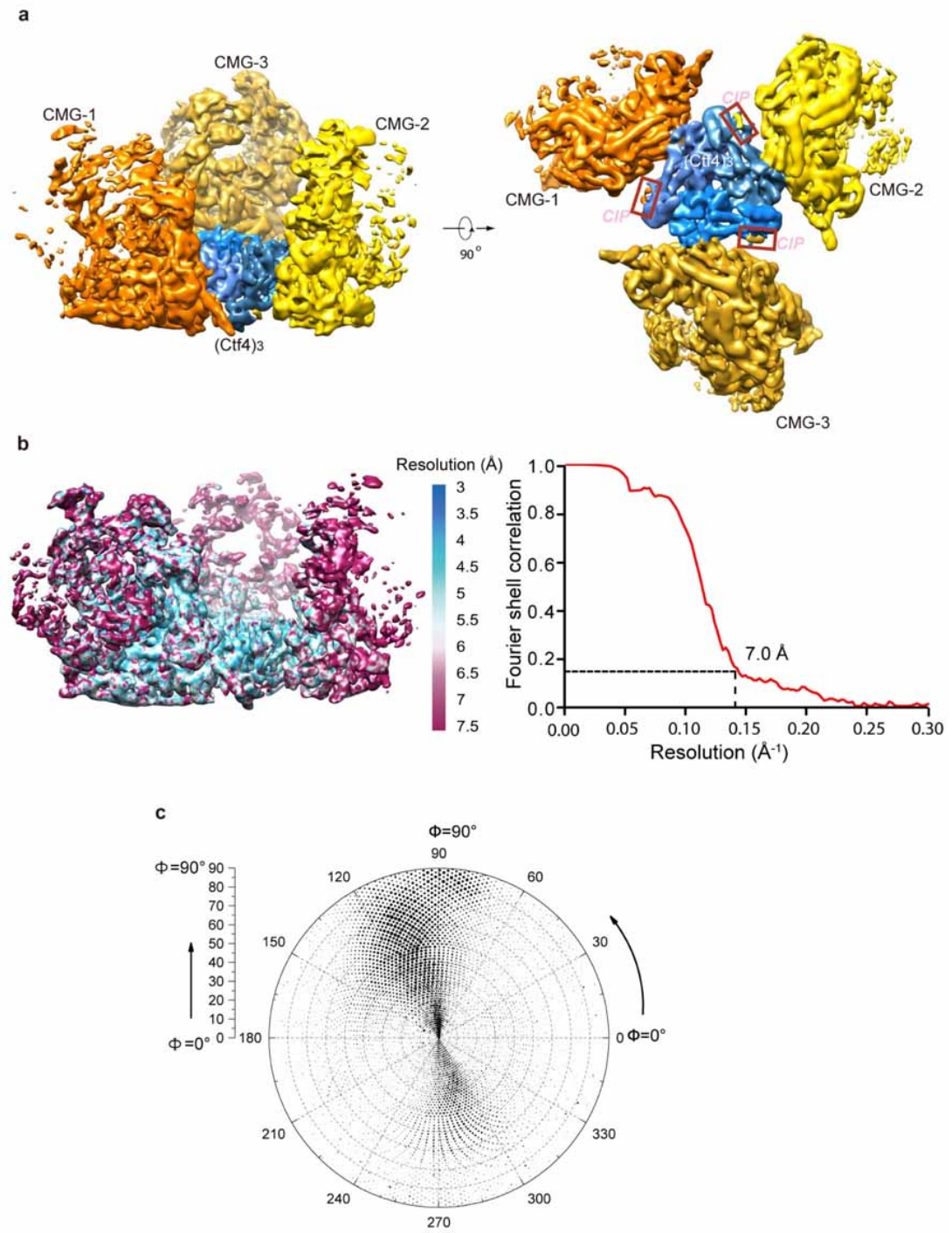

Figure 5 – figure supplement 2. 3D maps and resolution estimation of Ctf4$_3$ in complex with three CMG. (**a**) Surface-rendered 3D map of 3CMG-Ctf4$_3$ in side (left) and bottom (right, C-face of Ctf4$_3$). (**b**) Color-coded 3D map of 3CMG-Ctf4$_3$ according to the local resolution (left) and the gold-standard Fourier shell correlation of the two half maps. (**c**) Euler angle distribution of raw particles used in 3D reconstruction.

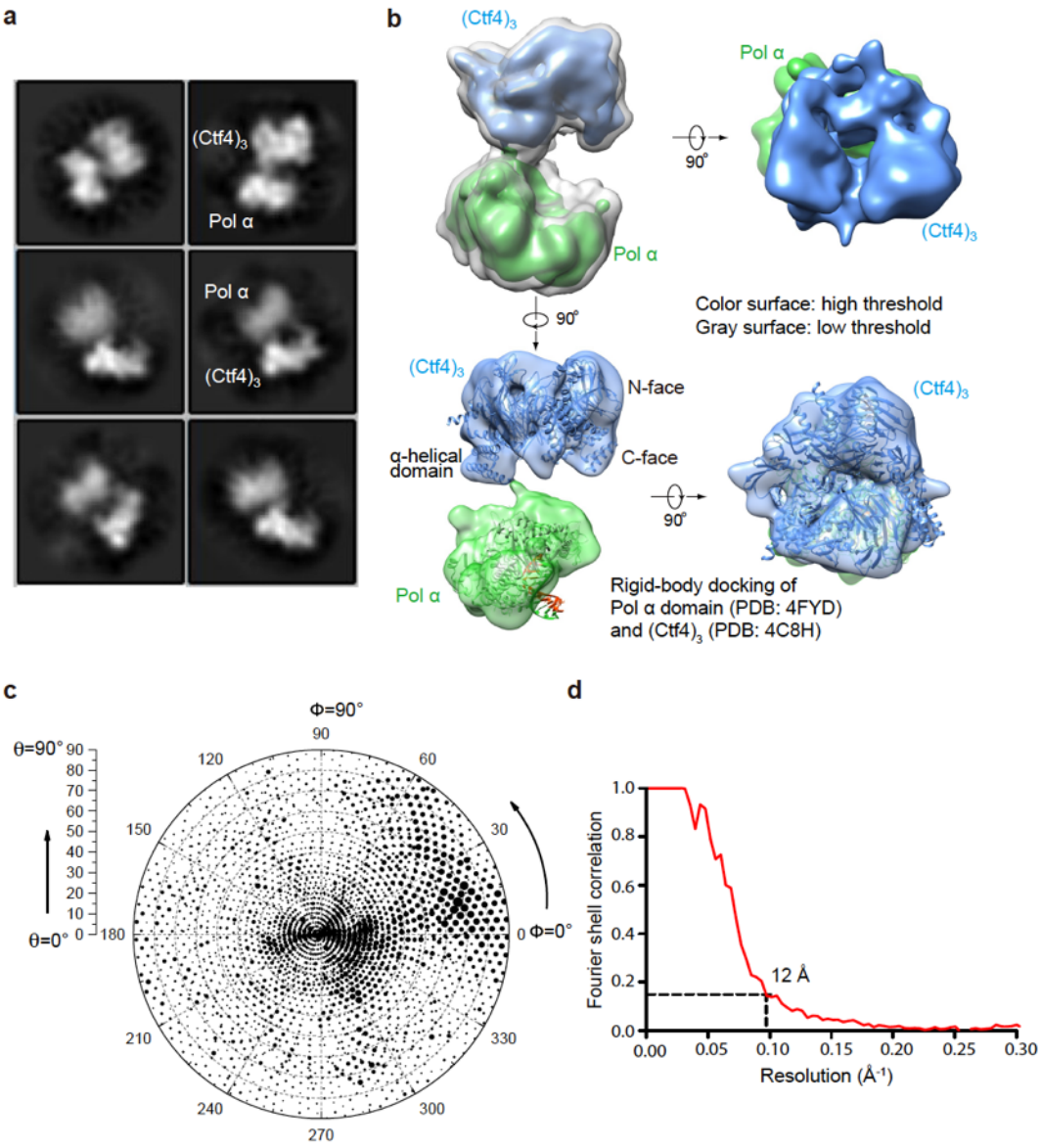

Figure 6 – figure supplement 1. Cryo-EM of the Pol1-Ctf4$_3$ complex. (**a**) 2D averages of Ctf4$_3$-Pol 1. (**b**) 2D classification reveals the presence of 1 Pol α bound to Ctf4$_3$. Side (left) and end-on (right) views of the 3D reconstruction of Pol 1-Ctf4$_3$ complex are shown. Only the Pol1 subunit (green) of Pol α-primase is observed with Ctf4$_3$ (blue) in the Pol α-primase-Ctf4$_3$ 3D reconstruction. In the end-on view, Pol1 appears to occlude the C-face of the Ctf4 trimer. The upper left structure shows both low and high thresholds, in grey and in color, respectively. The crystal structures of Pol1-DNA (4FYD) and the C-terminal half of Ctf4 (4C8H) were docked by rigid body docking of the unaltered crystal structures into semi-translucent views of the density at the bottom of panel b. **(c, d)** The Euler angle distribution and the FSC resolution curve are shown in panels c and d, respectively.

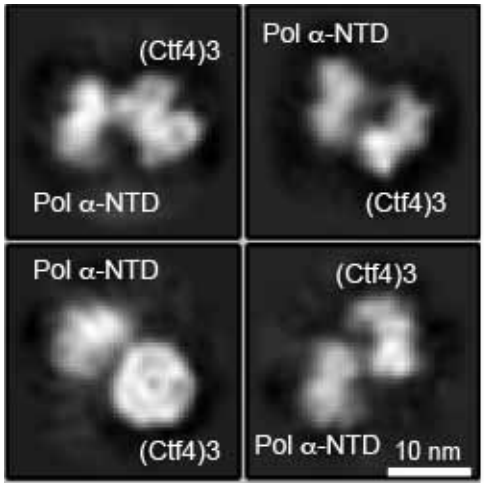

Figure 6 – figure supplement 2. Only one Pol α-primase is observed to bind to the Ctf4 trimer using 3 fold excess Pol α-primase to $Ctf4_3$. Cryo-EM 2D averages of protein mixtures containing $Ctf4_3$:Pol α-primase in a 1:3 molar ratio show no more than one Pol α-primase bound to $Ctf4_3$.

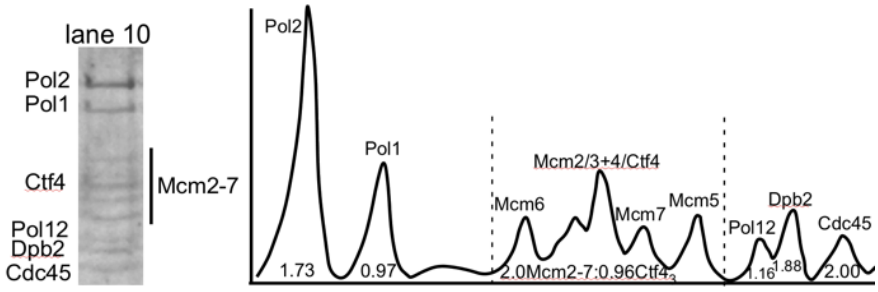

Figure 7 – figure supplement 1. Densitometry analysis of CMGE-Ctf4$_3$-Pol α-primase. Lane 10 of the SDS-PAGE of Figure S1a is shown to the left. The densitometry scan of the SDS gel lane 10 (right) was analyzed using ImageJ and indicates 2CMGE-1Ctf4$_3$-1Pol α-primase. The area of the Cdc45 peak was used as a proxy for CMG stoichiometry, and the area of the Cdc45 peak divided by the Cdc45 mw was assigned a value 2.0 because molar areas of Pol1, Pol12, and Ctf4$_3$ were about half the molar value of Cdc45. The amount of Ctf4$_3$, which overlaps Mcm4, was determined in two steps. First, the area of the Mcm2-7 region was divided by the molecular weight of Mcm2-7. The difference in area was deduced to belong to Ctf4$_3$, and calculated based on the molecular weight of a Ctf4 trimer. Calculated values are shown under the peaks. The stoichiometry approximates to 2 Cdc45 (and thus 2 Mcm2-7), 1 Ctf4$_3$, 1 Pol α, and 2 Pol ε.

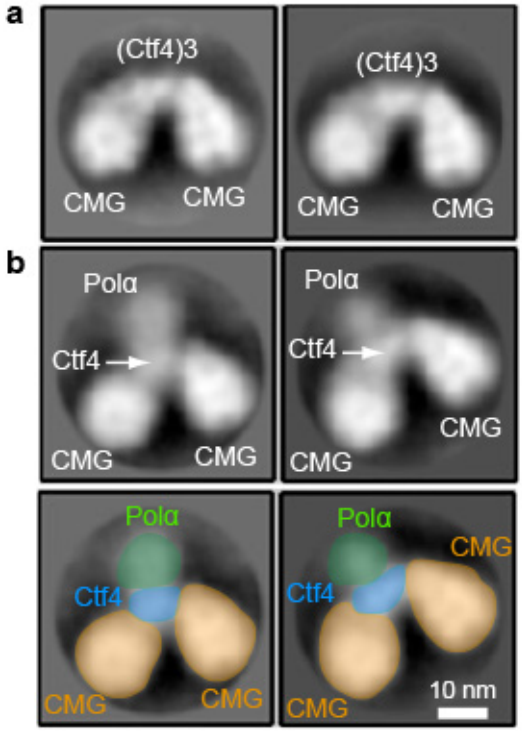

Figure 7 – figure supplement 2. EM observations of a 2CMG-Ctf4$_3$-1-Pol α-primase complex. (a) 2D class averages of negatively stained EM images of CMG plus Ctf4 trimer indicate a 2CMG-Ctf4$_3$ complex. (**b**) The top panels are 2D class averages of negatively stained EM images of a mixture of CMG, Ctf4 trimer and Pol α-primase, which we interpret as a complex of 2CMG-Ctf4$_3$-1Pol α-primase. The bottom panels explain the interpretation of the images in the top 2D averages of panel b using yellow to color CMGs, blue to color the Ctf4 trimer, and green to color the Pol1 subunit of Pol α -primase. See text for details.

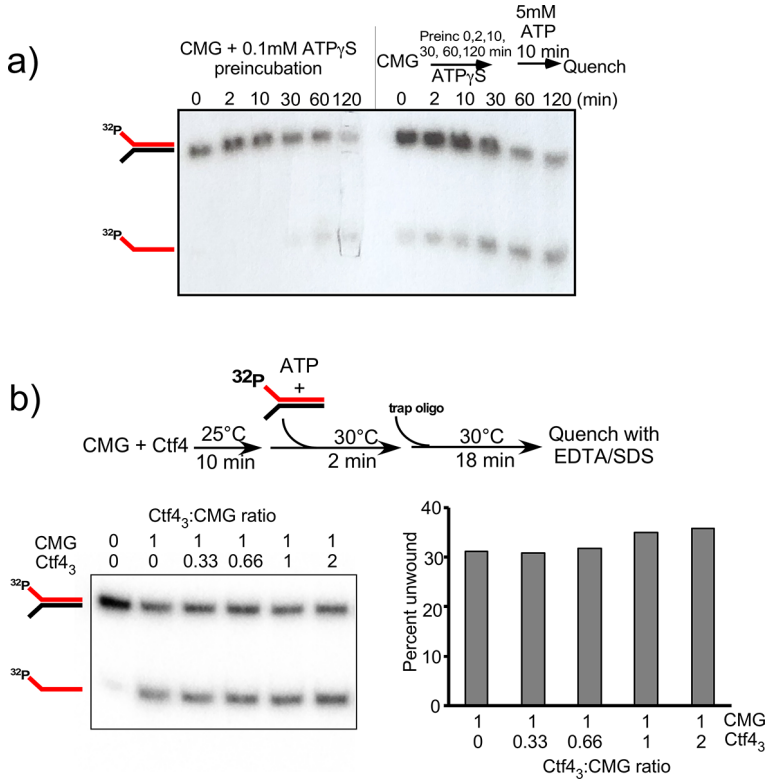

Figure 7 – figure supplement 3. Establishing preincubation conditions for CMG binding to DNA before adding ATP for unwinding in helicase assays. (a) Top: Native gel of the effect of preincubating DNA with CMG and 0.1 mM ATPγS for up to 120 min is shown in the left half of the gel. The right half shows the same preincubation with ATPγS followed by adding 5 mM ATP for 10 min before loading onto the gel. **(b)** Top: Scheme of the assay using CMG:Ctf4$_3$ formed using different ratios as indicated below. Helicase assays were performed by preincubating stock solution of CMG with Ctf4$_3$ to form the complex before adding 20 nM CMG in the CMG/Ctf4$_3$ mixture to reactions containing forked DNA having one strand 5' labeled with ^{32}P. Reactions were initiated upon adding DNA and 2 mM ATP, 50 nM unlabeled LEADING helicase oligo was added as a trap 2' after initiating the reaction, then reactions were quenched and analyzed by native PAGE. Bottom: Autoradiogram of the native PAGE (left). The histogram plot of the quantitation of the autoradiogram is shown to the right.

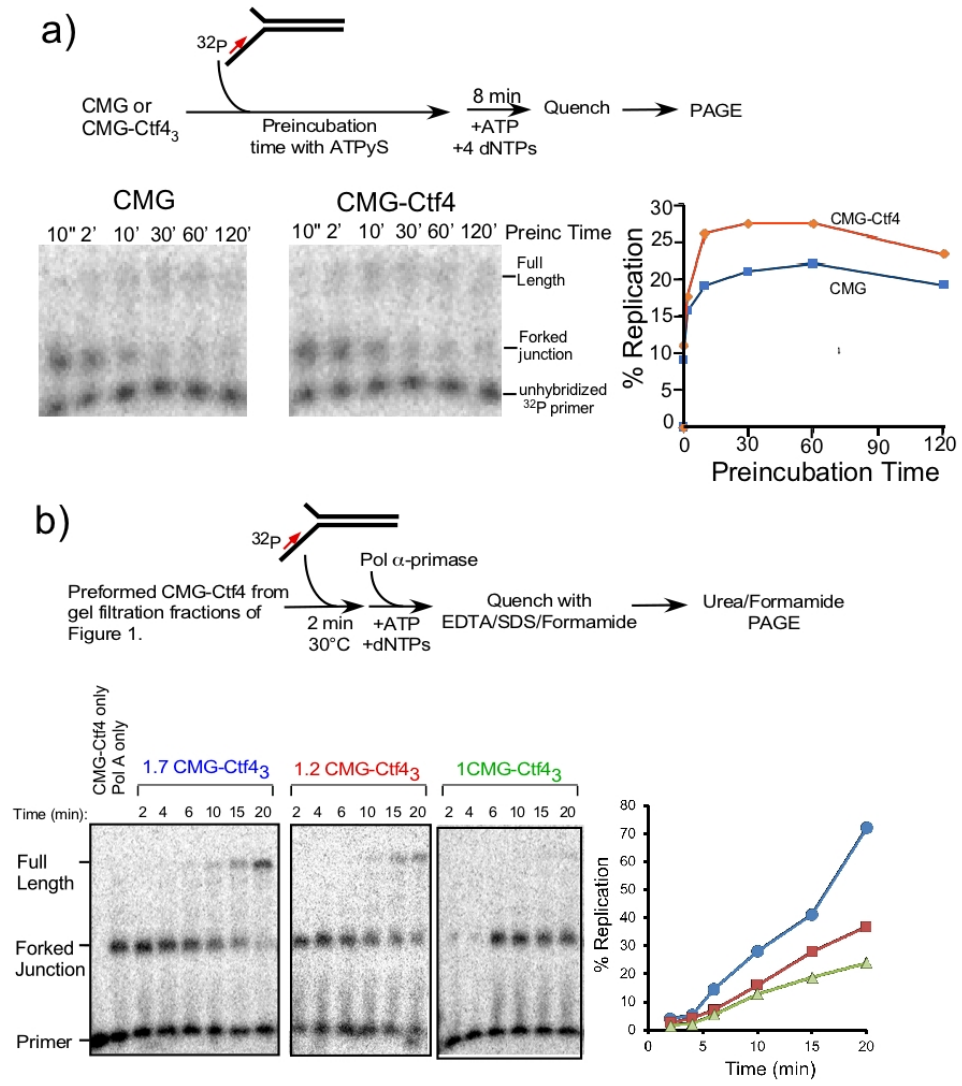

Figure 7 – figure supplement 4. Establishing preincubation conditions for CMG binding to primed fork DNA – before initiating DNA replication. (a) Top: scheme of the assay. Reactions containg reconstituted 20nM CMG +/- Ctf4 were preincubated with 0.5 nM ^{32}-P primed fork DNA and 100 μM ATPγS for the times indicated, followed by an 8 min pulse of replication using 5 mM ATP and 100 μM each dNTP. Bottom: results of the assays in denaturing PAGE (left) and quantitation (right). b) Replication results using isolated preformed CMG-Ctf4. Top: Scheme of the assay. 20 nM $Ctf4_3$ contained within either 1.7CMG-$Ctf4_3$ (fraction 31 from Fig. 1b), 1.2CMG-$Ctf4_3$ (fraction 35) or 1.0CMG-$Ctf4_3$ (fraction 37) were preincubated for 2 min with a ^{32}P-primed fork for 2 min, then 20 nM Pol α-primase was added for the times indicated in panel b, followed by quenching and analysis in a denaturing gel. **Bottom:** Denaturing PAGE of replication assays (left), and quantitation (right). It is important to note that because equal amounts of $Ctf4_3$ were added to the assays, a fraction containing 1.7 CMG:1$Ctf4_3$ has 1.7 times the CMG compared to a reaction containing 1.0 CMG:1$Ctf4_3$.

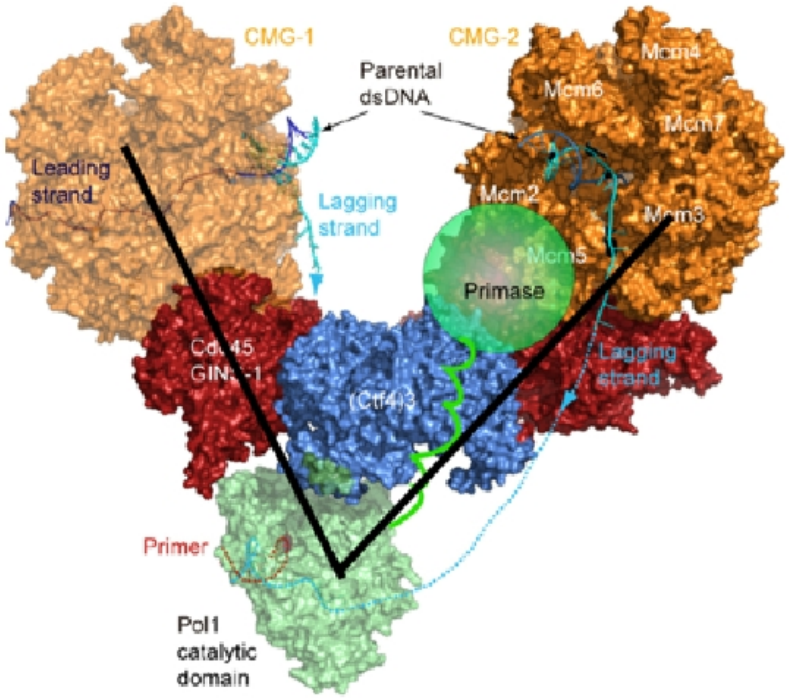

Figure 8 – figure supplement 1. The Pol1 and primase lobes of Pol α-primase have a 70° range of motion. The primase lobe of Pol α-primase is shown as a semi-transparent sphere connected to Pol1 by a flexible linker. Assuming the primase lobe extends past the Ctf4 disk and resides near the CMGs, the black lines indicate a 70° angle to approximate the previously documented range of motion between the Pol and primase lobes (Nunez-Ramirez et al., 2011).

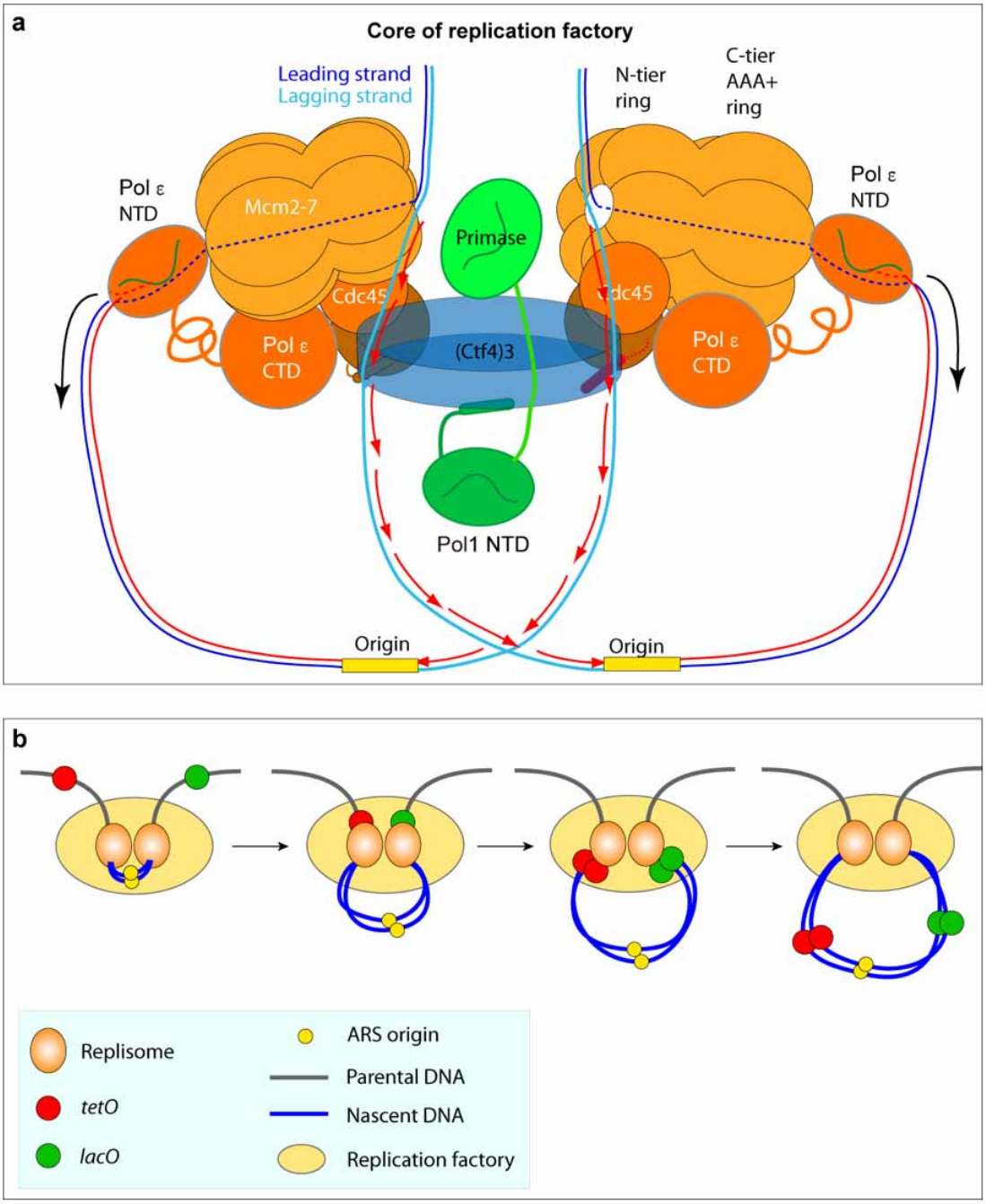

Figure 8 – figure supplement 2. Comparison of the proposed sister replisome core factory to conclusion of super-resolution imagine of marked DNA in cells. (a) Cartoon of the structural model of a core replicon factory from the current report, along with DNA produced from one bidirectional origin. The black arrows indicate the direction of duplicated leading strand DNA propelled from the leading strand Pol ε in the complex, and the red arrows correspond to the direction of lagging strand synthesis during Okazaki fragment extension. Panel **b** is adapted from **Fig. 1a** in Natsume and Tanaka, Chromosome Research, 2010, 18, 7-17.